SurEau-Ecos v2.0: A trait-based plant hydraulics model for simulations of plant water status and drought-induced mortality at the ecosystem level

Julien Ruffault[1], François Pimont[1], Hervé Cochard[2], Jean-Luc Dupuy[1] and Nicolas Martin-StPaul[1]

[1]INRAE, URFM, 84000 Avignon, France
[2]Université Clermont Auvergne, INRAE, PIAF, 63000 Clermont-Ferrand, France

Correspondence to: Nicolas Martin-StPaul (nicolas.martin@inrae.fr)

Abstract. A widespread increase in tree mortality has been observed around the globe, and this trend is likely to continue because of ongoing climate-induced increases in drought frequency and intensity. This raises the need to identify regions and ecosystems that are likely to experience the most frequent and significant damages. We present *SurEau-Ecos*, a trait-based, plant-hydraulic model designed to predict tree desiccation and mortality at scales from stand to region. *SurEau-Ecos* draws on the general principles of the process-based, soil-plant-atmosphere *SurEau* model. It also introduces a simplified representation of plant architecture and alternative numerical schemes; both additions made to facilitate model parameterization and large-scale applications. In *SurEau-Ecos*, the water fluxes from the soil to the atmosphere are represented through two plant organs (a leaf and a stem, which includes the volume of the trunk, roots and branches) as the product of an interface conductance and the difference of water potentials. Each organ is described by its symplasmic and apoplasmic compartments. The dynamics of plant's water status beyond the point of stomatal closure are explicitly represented via residual transpiration flow, plant cavitation and solicitation of plants' water reservoirs. In addition to the "explicit" numerical scheme of *SurEau*, we implemented a "semi-implicit" and "implicit" scheme. Both schemes led to a substantial gain in computing time compared to the "explicit" scheme (>10,000 times), and the implicit scheme was the most accurate. We also observed similar plant water dynamics between *SurEau-Ecos* and *SurEau* but slight disparities in infra-daily variations of plant water potentials that we attributed to the differences in the representation of plant architecture between models. A global model's sensitivity analysis revealed that factors controlling plant desiccation rates differ depending on whether leaf water potential is below or above the point of stomatal closure. Total available water for the plant, leaf area index, and the leaf water potential at 50% stomatal closure mostly drove the time needed to reach stomatal closure. Once stomata are closed, resistance to cavitation, residual cuticular transpiration and plant water stocks mostly determined the time to hydraulic failure. Finally, we illustrated the potential of *SurEau-Ecos* to simulate regional drought-induced mortality over France. *SurEau-Ecos* is a promising tool to perform regional-scale predictions of drought-induced hydraulic failure, determine the most vulnerable areas and ecosystems to drying conditions, and asses the dynamics of forest flammability.

1. Introduction

Forests across many regions worldwide are experiencing record-breaking droughts followed by widespread increase in climate-driven disturbance events, including tree mortality (Allen et al., 2015; Fettig et al., 2019; Schuldt et al., 2020), wildfires (Abram et al., 2021; Ruffault et al., 2020) and insect outbreaks (Jactel et al., 2012). Droughts are likely to become more frequent and more intense over the next decades because of the global increase in temperatures and heatwaves coupled, in some regions, to some changes in the hydrological cycle (Trenberth et al., 2014). Given the importance of forests for biochemical cycles and ecosystem services (Seidl et al., 2014), there is a growing need for the development of models that can simulate the response of forests to extreme drought. Process-based vegetation models can help to address these issues because they represent the mechanisms governing plant physiological responses to drought and account for the interspecific and intraspecific variations of tree traits and their potential acclimation to a rapidly changing climate.

The science of plant hydraulics seeks to understand the physical and physiological mechanisms driving water transport in plants. This research field has proven to be a relevant theoretical framework to study the effect of global changes on plant and the terrestrial water cycle (Brodribb et al., 2020; Choat et al., 2018). Advances in plant hydraulic modelling have accelerated over the last two decades (Fatichi et al., 2016; Mencuccini et al., 2019) and used as mean to tackle diverse prediction challenges, such as tree mortality (De Kauwe et al., 2020; Venturas et al., 2020), water use efficiency (De Cáceres et al., 2021; Domec et al., 2017) or species distribution (Sterck et al., 2011). Many of SPA models were also designed (or reformatted) to be integrated into land-surface models and improve the representation of the feedbacks between land and climate systems (Christoffersen et al., 2016; Kennedy et al., 2019; Li et al., 2021; Xu et al., 2016). Recently, modeling water transport in plants also proved to be a promising way to assess the seasonal dynamics of live fuel moisture (foliage and twigs water content, dead to live fuel ratio), a key variable for fire behavior that could play a major role in raising forests' flammability under climate warming (Nolan et al., 2020; Ruffault et al., 2018).

Most plant hydraulic models represent water fluxes in plants through a mathematical approach of soil-plant-atmosphere continuum, wherein diffusion laws control the water flow through the soil, root, and leaves (Mencuccini et al., 2019). Water flow through plants is considered as being analogous to the electric current through a circuit with a series of resistance and/or capacitance (Sperry et al., 1998). SPA models, however, vary widely in their complexity, some of them representing trees as a single resistance (Mackay et al., 2003; Williams et al., 1996), while others include multiple resistances and capacitances (Couvreur et al., 2018; Sperry et al., 1998; Tuzet et al., 2017). How physiological processes regulate plant transpiration also differs between SPA models (Mencuccini et al., 2019). Some models describe stomatal conductance through semi-empirical models (Christoffersen et al., 2016; Feng et al., 2018; Li et al., 2021; Williams et al., 1996) while others are based on optimality approaches (Sperry et al., 2017; Wang et al., 2020).

The *SurEau* SPA model was developed specifically to simulate plant desiccation under extreme drought and heatwaves (Cochard et al., 2021; Martin-StPaul et al., 2017). As other SPA models, *SurEau* describes the soil-plants-atmosphere system as a network of resistances and capacitances and computes water exchanges until stomatal closure.
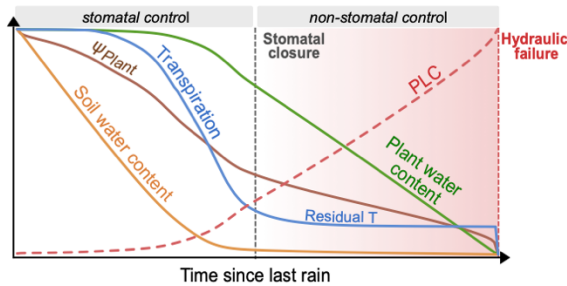
Additionally, *SurEau* simulates plant tissue desiccation beyond the point of stomatal closure by accounting for residual plant transpiration and the discharge of internal plant water stores (Fig. 1a). Unlike most current approaches (e.g., Tuzet et al., 2017;

65 Xu et al., 2016), *SurEau* explicitly accounts for the differences in capacitance of the symplasmic and apoplasmic compartments, which can be calibrated, from pressure-volume curves for the symplasm and vulnerability curves for the apoplasm. Symplasmic capacitances mostly buffer water fluxes during well-watered conditions, whereas apoplasm capacitances come into play when cavitation occurs (Fig. 1a). Thus, *SurEau* accounts for the leading role of cavitation in the dynamics of plant desiccation (Mantova et al., 2021) and the probability of plant mortality (Adams et al., 2017). *SurEau* has

70 been successfully evaluated against field cavitation observations (Cochard et al. 2021; hereafter CPRM21), applied in different contexts (Lemaire et al., 2021; López et al., 2021), and performed well in predicting plant water fluxes when compared to other plant hydraulic models (Mcdowell et al., in press).

As noted in CPRM21, two *SurEau*'s characteristics impede its use for large-scale ecological applications or its integration into terrestrial biosphere models. First, SurEau requires a high number of parameters because of its detailed representation of plant

75 architecture, and of the mechanisms involved in plant water exchanges. The second limitation of *SurEau* is its high computation time, which is partly due to the use of a first-order "explicit" numerical scheme to compute water flows. This scheme requires that variations in water quantities be computed at very small-time steps to avoid numerical instabilities due to the Courant-Friedrichs-Lewy condition (CFL; Dutykh, 2016). A numerical method has been proposed to overcome these instabilities and increases the time step (Tuzet et al., 2017; Xu et al., 2016) but this is not directly compatible with *SurEau*'s specificities

80 regarding capacitances and cavitation. Moreover, knowledge regarding numerical physics and methods for simulation have seldom been applied to plant hydraulics.
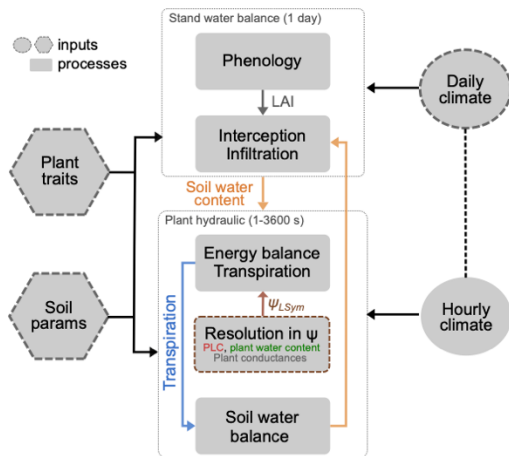
We present *SurEau-Ecos,* a new SPA model meant to improve the predictions of ecosystems' transpiration, desiccation and drought-induced mortality at scales from stand to region. *SurEau-Ecos* draws on the physiological and physical framework of *SurEau* while limiting the number of parameters and reducing computational cost. In the following sections, we first describe

85 the principles, functioning, main equations and numerical schemes of *SurEau-Ecos*. Second, we compare simulations produced with three numerical schemes (Explicit, Semi-implicit and Implicit) in terms of predictions' stability and computing time. Third, we further describe the differences in plant hydraulic architecture between *SurEau-Ecos* and *SurEau* (CPRM21) and their impacts on simulation results. Fourth, we perform a global sensitivity analysis of tree desiccation dynamics to the main *SurEau-Ecos* input, i.e., plant hydraulic traits and stand and soil parameters. Fifth, we illustrate the potentialities which *SurEau-*

90 *Ecos* will provide by running prospective simulations of hydraulic failure probability at the regional scale under changing climate.
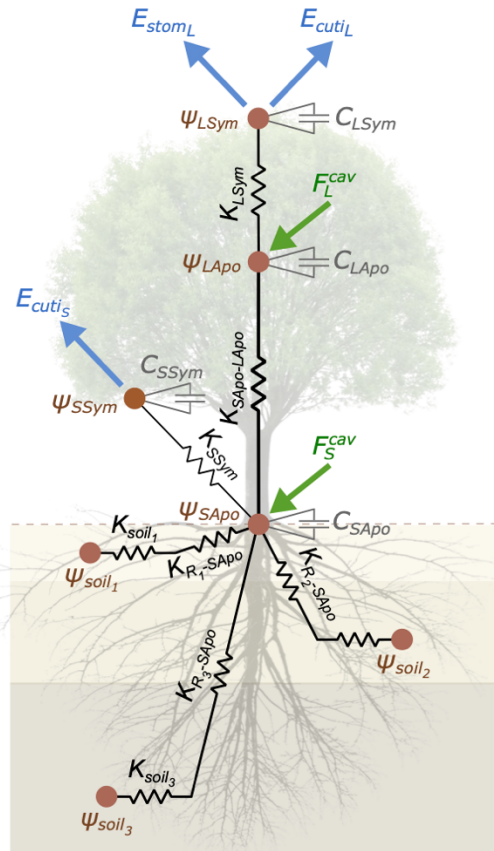
Fig. 1: Overview of the *SurEau-Ecos* plant-hydraulic model. (a) Schematic trajectories of the main processes involved in drought-induced tree mortality under extreme drought. In a first phase, stomata are open and transpiration gradually empty soil water reservoirs. Then stomata gradually close as water potential decreases. In a second phase, once stomata are fully closed, only residual transpiration (equivalent to cuticular transpiration in the model) remains. Percent loss of conductivity (PLC) increases and the plant mostly rely on internal water reservoirs until hydraulic failure. (b) Simplified workflow of *SurEau-Ecos*. Key modules and their interactions are shown by arrows and boxes. (c) Schematic representation of the plant hydraulic architecture in *SurEau-Ecos*.

2. Description of SurEau-Ecos

2.1 Model overview

SurEau-Ecos is a plant hydraulic model that simulates water fluxes between the soil, plant and atmosphere for a monospecific layer of vegetation. In *SurEau-Ecos* the soil-plant system is discretized into three soil layers and two plants compartments: a leaf and a "stem" (Fig. 1c). Each of the two plant organs contains an apoplasm and a symplasm. The stem apoplasm and symplasm include water volumes of all non-leaf compartments, i.e., trunk, root and branches.

Geoscientific
Model Development
Discussions

105 Water dynamics of the soil-plant-atmosphere system (represented by nodes in Fig. 1c) are locally governed by a generic partial
differential equation for water mass conservation:

$$\frac{dq}{dt} = \nabla.(k\nabla\psi) + s \qquad (1)$$

where q is the local water content, k the conductivity, ψ the water potential, $k\nabla\psi$ the water fluxes and s the local sink term
(i.e., a negative sign for soil evaporation or transpiration) or source term (i.e., a positive sign for precipitation and water released
110 by cavitation).

A spatially-integrated form of Eq. (1) can be specified for each compartment of the plant (Fig. 1c) to derive the rate of change
of its total water content. To account for the water fluxes between compartments and for the contribution of internal water
stocks (i.e., capacitances). The computations of water fluxes between two adjacent compartments ($F_{i\rightarrow j}$) are simulated
according to Darcy's law as the product of compartment' interface conductance (K_{ij}) and the gradient of water potential (ψ) :

$$F_{i\rightarrow j} = k_{ij}\nabla\psi \approx K_{ij}(\psi_j - \psi_i) \qquad (2)$$

115 These fluxes are described in Sect. 2.3.

In addition, solving Eq. 1 needs to describe the link between Q and ψ. This is handled using the notion of capacitance for the
plant compartments and water retention curves for the soil compartments. Plant capacitances (C) are defined as:

$$C = \frac{dQ}{d\psi} \qquad (3)$$

For any plant compartments a generic equation of the water balance can now be written:

$$C\frac{d\psi_i}{dt} + \sum_j K_{ij}(\psi_i - \psi_j) - S = 0 \qquad (4)$$

According to the type of compartment, S includes cuticular or stomatal transpiration losses or water release from cavitation
120 which is also accounted as a source term in the apoplasm (Cruiziat et al., 2002). Cuticular or stomatal transpiration fluxes are
computed differently for each compartment (leaf symplasm includes stomatal transpiration whereas stem symplasm only
include cuticular transpiration). The contribution of capacitance (C) to the plant compartment water balance is related to the
saturated (or initial) water quantity (Q^{sat}) in that compartment and takes different formulation for symplasm and apoplasm. A
pressure-volume curve is used for the symplasmic capacitance (Tyree and Hammel, 1972) whereas a constant capacitance is
125 used for the apoplasm (Sec. 2.5). To the best of our knowledge, this is the first formulation of symplasmic C and cavitation
flux as Darcy's law (see details in Sec. 2.3.3. and 2.5.1). These generic forms are needed for the numerical resolution of water
balance at each plant node (described in Sect. 2.2.1).

For soil compartments, the water balance of a soil layer j is computed using a generic equation following Eq. 1 and 2 such as:

$$\frac{dQ_{soil_j}}{dt} + K_{soil_j-SApo}\left(\psi_{soil_j} - \psi_{SApo}\right) - S = 0 \tag{5}$$

Where K_{soil_j-Sapo} is the conductance from the soil layer j to the stem apoplasm (Sect. 2.3.1). S represents a source (when S>0)

130 or sink (when S<0) term that can include soil water inputs from soil infiltration, drainage from other layer or outputs such as deep drainage, soil evaporation or capillarity depending on the soil layer (Sect. 2.2.2). A water retention curve for the soil (van Genuchten, 1980) is used to link Q_{soil_j} and ψ_{soil_j} and solve eq. 5 (Sect. 2.5.2).

In addition to the core soil-plant hydraulic processes driving transpiration and plant water status (Q and ψ), SurEau-Ecos also includes an empirical module for leaf phenology that control leaf area growth and decrease during senescence (described in

135 Appendix A) and different modules to represent the stand water balance (interception, water transfers between soil layers and drainage; described in Ruffault et al. 2013). The list of input variables and their respective unit is given in Tab. 1.

Temporal resolution varies according to each type of process (Fig. 1b). Phenology and stands water balance are computed at a daily time step. Soil-plant hydraulics processes (i.e., soil water uptake, transpiration and hydraulic redistribution) are computed at the finer time step (from 0.01 to 1800 s depending on the resolution scheme) and driven by hourly interpolated

140 climate, which is derived from daily climate following De Cáceres et al., (2021) (See Tab. B1 for the list of daily input weather variables). The three different numerical resolution schemes currently implemented in *SurEau-Ecos* are described in Sect. 2.6. All variables and processes related to stand water balance processes (precipitation, interception, drainage) are expressed per unit ground surface area, while plant hydraulic processes are expressed per unit leaf surface area, in accordance with usual practices in each research field. This implicates that initial water volumes of the soil and the plant (leaf and stem) are expressed

145 per unit soil area. Then, leaf area index (LAI) permits to convert quantities from a soil area basis to a leaf area basis. If the parametrization is performed from individual tree dimensions or from forest inventories and allometries, an additional parameter is needed, the average plant foot print (*aPFP,* in m^2), in order to scale individual plant dimensions on leaf or a soil area basis.

SurEau-Ecos was implemented in the *R* programming language (R Core Team, 2020). The following sections describe the

150 equations and resolution of the model in more details.

Geoscientific
Model Development
Discussions

	Parameter	Description	Unit
Stand	LAI_{max}	Maximum leaf area index of the stand	$m^2_{leaf}.m^{-2}_{soil}$
	t_0	Initial date of the forcing period for leaf phenology	DOY
	T_D	Minimum temperature to start cumulating temperature for budburst	$°C$
	F^*	Amount of forcing temperature to reach budburst	$°C$
	R_{LAI}	LAI growth rate per day	$LAI.day^{-1}$
	cws	Canopy water storage capacity	$mm.LAI^{-1}$
	k	Light extinction parameter	-
Plant	ε_L	Modulus of elasticity of the leaf symplasm	MPa
	π_{0_L}	Osmotic potential at full turgor of the leaf symplasm	MPa
	ε_S	Modulus of elasticity of the stem symplasm	MPa
	π_{0_S}	Osmotic potential at full turgor of the stem symplasm	MPa
	$slope_L$	Slope of rate of leaf embolism spread at $\psi_{50,L}$	$\%.MPa^{-1}$
	$\psi_{50,L}$	Water potential causing 50% loss of leaf hydraulic conductance	MPa
	$slope_S$	Slope of rate of stem embolism spread at $\psi_{50,S}$	$\%.MPa^{-1}$
	$\psi_{50,S}$	Water potential causing 50% loss of stem hydraulic conductance	MPa
	$K_{R-SApo,max}$	Maximum conductance from the root surface to the stem apoplast	$mmol.m^{-2}_{leaf}.s^{-1}.MPa^{-1}$
	$K_{SApo-LApo,max}$	Maximum conductance from trunk apoplasm to the leaf apoplasm	$mmol.m^{-2}_{leaf}.s^{-1}.MPa^{-1}$
	K_{SSym}	Conductance from the stem apoplasm to stem symplasm	$mmol.m^{-2}_{leaf}.s^{-1}.MPa^{-1}$
	K_{LSym}	Conductance from the leaf apoplasm to leaf symplasm	$mmol.m^{-2}_{leaf}.s^{-1}.MPa^{-1}$
	α_{LApo}	Leaf apoplasmic fraction	-
	α_{SApo}	Stem apoplasmic fraction of the wood water volume	-
	α_{SSym}	Stem symplasmic fraction of the wood water volume	-
	C_{LApo}	Capacitance of the leaf apoplasm	$mmol.m^{-2}_{leaf}.MPa^{-1}$
	C_{SApo}	Capacitance of the stem apoplasm	$mmol.m^{-2}_{leaf}.MPa^{-1}$
	V_S	Volume of tissue of the stem (includes the root, trunk and branches)	$L.m^{-2}_{soil}$
	$Succulence$	Leaf succulence (water content per unit leaf area)	$g.m^{-2}_{leaf}$
	$LDMC$	Leaf dry mater content (dry mass over saturated mass)	$g.g^{-1}$
	LMA	Leaf mass per area	$g.m^{-2}_{leaf}$
	β	Shape parameter for root distribution	-
	$RaLa$	Root to leaf area ratio	-
	d_R	Root diameter	m
	ψ_{gs50}	Water potential causing 50% stomatal closure	MPa
	$slope_{gs}$	Rate of decrease in stomatal conductance at $\psi_{gs,50}$	$\%.MPa^{-1}$
	g_{stom_min}	Minimum stomatal conductance	$mmol.m^{-2}_{leaf}.s^{-1}$
	g_{stom_max}	Maximum stomatal conductance	$mmol.m^{-2}_{leaf}.s^{-1}$
	δ	Response of g_{stom} to light	-
	T_{optim}	Temperature at maximal stomatal conductance	$°C$
	T_{sens}	Stomatal sensitivity to temperature	$°C$
	g_{crown0}	Reference crown conductance	$mmol.m^{-2}_{leaf}.s^{-1}$
	g_{cuti20}	Cuticular conductance at 20°C	$mmol.m^{-2}_{leaf}.s^{-1}$
	Q_{10a}	Temperature dependance of g_{cuti} when $T \leq T_{Phase}$	-
	Q_{10b}	Temperature dependance of g_{cuti} when $T > T_{Phase}$	-
	T_{Phase}	Temperature for transition phase of g_{cuti}	$°C$
Soil	rfc_j	Rock fragment content of layer j	$\%$
	d_j	Maximum depth of layer j	m

Geoscientific
Model Development
Discussions

θ_s	Soil water content at saturation	-
θ_r	Residual soil water content	-
α	Inverse of the air entry potential	MPa^{-1}
n	Pore size distribution index	-
l	Shape parameter for the Van Genuchten equation	-
k_{sat}	Soil hydraulic conductivity at saturation	$mmol.m_{soil}^{-1}.s^{-1}.MPa^{-1}$
g_{soil0}	Reference soil conductance to water vapor	$mmol.m_{soil}^{-2}.s^{-1}$

Tab. 1: Input parameters in *SurEau-Ecos*.

2.2. Water balance in each compartment

155 **2.2.1. Plant**

The water balance of each of the four-plant compartment (leaf and stem symplasm and apoplasm, Fig. 1c) is determined according to the generic Eq. 4 and solved at each time step.

For the leaf apoplasm, the water balance equation is:

$$\underbrace{C_{LApo}\frac{d\psi_{LApo}}{dt}}_{Water\ quantity\ change} + \underbrace{K_{SApo-LApo}\left(\psi_{LApo}-\psi_{SApo}\right)}_{Flux\ to\ stem\ apoplasm} + \underbrace{K_{LSym}\left(\psi_{LApo}-\psi_{LSym}\right)}_{Flux\ to\ leaf\ symplasm} - \underbrace{F_L^{cav}}_{Cavitation} = 0 \qquad (6)$$

The first term represents the change in water quantity related to the leaf apoplasmic capacitance ($C_{LApo}, mmol.m_{leaf}^{-2}.MPa^{-1}$)

160 which releases or absorbs water according to volume changes due to water potential changes (ψ_{LApo}, MPa). Contrary to symplasmic compartments, this term is very limited in the apoplasm because by xylem wall is inelastic. Note also that cavitation is not included in this capacitance. The second and third terms are the water exchanges between the leaf apoplasm and stem apoplasm and between the leaf apoplasm and leaf symplasm, respectively. ψ_{SApo} is the water potential of the stem apoplasm, ψ_{LSym} is the water potential of the leaf symplasm, $K_{SApo-LApo}$ ($mmol.m_{leaf}^{-2}.s^{-1}.MPa^{-1}$) is the conductance from

165 the stem apoplasm to leaf apoplasm and K_{LSym} is the conductance of the leaf symplasm. This equation applies to the non-cavitated part of the xylem, which receives water from the cavitated part. This source is represented by the fourth term F_L^{cav} ($mmol$), which corresponds to the water release by the cavitated vessels towards the non-cavitated leaf apoplasm (Hölttä et al., 2009). This term is further described in Sect. 2.3.2, where we explain how it can be expressed as a function of ψ_{LApo}.

Water balance for the stem apoplasm:

$$\underbrace{C_{SApo}\frac{d\psi_{SApo}}{dt}}_{Water\ quantity\ change} + \underbrace{\sum_j K_{soil_j-SApo}\left(\psi_{SApo}-\psi_{soil_j}\right)}_{Flux\ to\ soil\ layers} + \underbrace{K_{SApo-LApo}\left(\psi_{SApo}-\psi_{LApo}\right)}_{Flux\ to\ leaf\ apoplasm} + \underbrace{K_{SSym}\left(\psi_{SApo}-\psi_{SSym}\right)}_{Flux\ to\ stem\ symplasm} - \underbrace{F_S^{cav}}_{Cavitation} = 0 \qquad (7)$$

170 The first term represents the water flux related to the stem apoplasmic capacitance (C_{SApo}) and water potential (ψ_{SApo}) changes during the time step. As with the leaf apoplasm, this term is in general very limited for the stem apoplasm. The second term represents the water exchange between the stem apoplasm and the three soil layers. For each soil layer j, K_{soil_j-SApo} is the conductance from the soil to the stem apoplasm and ψ_{s_j} the soil water potential. The third and fourth terms represent flux to

the leaf apoplasm and stem symplasm, respectively. ψ_{SSym} is the water potential of the stem symplasm and K_{SSym} is the stem-

175   symplasm conductance. The fifth term F_S^{cav} , corresponds to the water released from cavitation to the non-cavitated stem apoplasm water reservoir.

Water balance for the leaf symplasm:

$$\underbrace{C_{LSym}\frac{d\psi_{LSym}}{dt}}_{Water\ quantity\ change} + \underbrace{K_{LSym}\big(\psi_{LSym} - \psi_{LApo}\big)}_{Flux\ to\ leaf\ apoplasm} + \underbrace{E_{stom}}_{Stom\ transpiration} + \underbrace{E_{cuti_L}}_{Leaf\ cuticular\ transpiration} = 0 \qquad (8)$$

The first term represents the water flux related to C_{LSym} and water potential changes of the leaf symplasm (ψ_{LSym}) during the time step. The second term is the exchange between leaf apoplasm leaf symplasm. The third and fourth terms represent the

180   losses of water from the plant to the atmosphere, through leaf stomatal transpiration (E_{stom}) and cuticular leaf transpiration (E_{cuti_L}). Note that with this formulation, leaf water losses from leaf transpiration remains lower-bounded by E_{cuti_L} even when stomata are fully closed ($E_{stom} = 0$)

Water balance for the stem symplasm:

$$\underbrace{C_{SSym}\frac{d\psi_{Ssym}}{dt}}_{Water\ quantity\ change} + \underbrace{K_{SSym}\big(\psi_{SSym} - \psi_{SApo}\big)}_{Flux\ to\ stem\ apoplasm} + \underbrace{E_{cuti_S}}_{Stem\ cuticular\ transpiration} = 0 \qquad (9)$$

The first term represents the water flux related to C_{SSym} and water potential changes of the stem symplasm (ψ_{SSym}) during the

185   time step. The second term is the flux to the stem apoplasm. The third and fourth terms represent the losses of water from the plant to the atmosphere, through minimum cortical transpiration (E_{cuti_S}).

2.2.2 Soil

The water balance of each of the three soil layers (Fig. 1c) is determined according to the generic equation 5 and solved at each time step.

190   For the first soil layer:

$$\frac{dQ_{soil_1}}{dt} + \underbrace{k_{soil_1-SApo}\big(\psi_{soil_1} - \psi_{SApo}\big).LAI}_{Flux\ to\ Stem\ Apoplasm} + ppt_{soil} - D_{1\to2} - E_{soil} = 0 \qquad (10)$$

The first term ($\frac{dQ_{soil_1}}{dt}, mmol.m_{soil}^{-2}$) represents the change in soil water quantity between two consecutive time steps. The second term is the flux to the stem apoplasm. This flux is multiplied by LAI to convert water quantities from a leaf area basis to a soil area basis. ppt_{soil} ($mmol.m_{soil}^{-2}$) is the precipitation reaching the soil. $D_{1\to2}$ the drainage ($mmol.m_{soil}^{-2}$) of the first to the second layer, and $E_{soil}(mmol.m_{soil}^{-2})$ is soil evaporation that occurs only from this layer.

195   Similarly, for the second layer:

$$\frac{dQ_{soil_2}}{dt} + \underbrace{K_{soil_2-SApo}\big(\psi_{soil_2} - \psi_{SApo}\big).LAI}_{Flux\ to\ Stem\ Apoplasm} + D_{1\to2} - D_{2\to3} = 0 \qquad (11)$$

For the third soil layer:

$$\frac{dQ_{soil_3}}{dt} + \underbrace{K_{soil_3-SApo}(\psi_{soil_3} - \psi_{SApo}).LAI}_{\text{Flux to Stem Apoplasm}} + D_{2\rightarrow3} - Dd = 0 \tag{12}$$

Where Dd is the deep drainage ($mmol.m_{soil}^{-2}$). For any layer, drainage occurs when the field capacity of the soil layer (θ_{fc}) is overpassed. Lateral water transfer processes and upward capillary transfers between layers are neglected. At the time step of the hydraulic model (dt) the water balance of each soil layer is treated according to the losses from transpiration and from

200 evaporation (only for the first layer). Incoming fluxes from precipitation, drainage and transfers between soil layers are treated at a daily time step (Fig. 1b). Rainfall interception and drainage are treated as in SIERRA (Mouillot et al., 2001; Ruffault et al., 2013), and follows the design principles of several other water balance models (De Cáceres et al., 2015; Granier et al., 1999; Rambal, 1993).

2.3 Conductances and fluxes

205 **2.3.1 Plant and soil conductances**

The model includes four apoplasmic conductances (three root-to-stem and one stem-to-leaf), two symplasmic conductances (one for the stem and one for the leaves) and three soil conductances (one per soil layer) (Fig. 1c). Symplasmic conductances of the leaves (K_{LSym}) and stem (K_{SSym}) drive the fluxes between the symplasmic and apoplasmic compartments. These conductances are set at a constant value throughout the simulation. Xylem (i.e., apoplasmic) conductances are composed of

210 three root-to-stem conductances in parallel (one per soil layer) and of a trunk-to-stem conductance. These conductances can vary throughout the simulation from their initial value down to 0 according to the level of cavitation (expressed by the percent loss in conductance).

The stem-to-leaf apoplasmic conductance ($K_{SApo-LApo}$) is expressed as a function of the percent loss of conductance due to xylem embolism in the leaf:

$$K_{SApo-LApo} = K_{SApo-LApo,max} \frac{100 - PLC_L}{100} \tag{13}$$

215 Where $k_{SApo-LApo,max}$ is the initial (maximum) root to leaf conductance and $PLC_L(\%)$ is the percent loss of conductance. PLC_L is proportional to the level of xylem embolism. It occurs when the water potential drops below the capacity of the leaf xylem to support negative water potential and is computed by using the sigmoidal function (Pammenter and Vander Willigen, 1998) :

$$PLC_L = \frac{100}{1 + e^{\left(\frac{slope_L}{25}.(\psi_{LApo}-P_{50,L})\right)}} \tag{14}$$

Where $P_{50,L}$ (MPa) is the water potential causing 50% loss of plant hydraulic conductance and $slope_L$ (%/MPa) is the slope of

220 linear rate of embolism spread per unit water potential drop at the inflexion point $P_{50,L}$.

The apoplasmic conductance from each root j to the stem apoplasm (K_{R_j-SApo}) is expressed as a function of the level of embolism computed at the node of the stem apoplasm:

$$K_{R_j-SApo} = K_{R_j-SApo,max} \frac{100 - PLC_{SApo}}{100} \tag{15}$$

Where PLC_S is computed as PLC_L with the stem apoplasmic potential (ψ_{SApo}) and vulnerability curves parameters specific to the stem ($slope_S$ and $P_{50,S}$). $K_{R_j-SApo,max}$ is the maximal root-to-stem apoplasmic conductance of layer j. It is derived from

225   fine root area of the layer j such as:

$$K_{R_j-SApo,max} = RAI_j \times K_{R-SApo} \tag{16}$$

Where K_{R-SApo} is the total conductance of the root system. RAI_j is the fine root area of the layer j:

$$RAI_j = RAI \times r_j \tag{17}$$

Where RAI is the total fine root area which is computed from the stand leaf area index and the root to leaf area ratio $RaLa$; and r_i the root fraction in each soil layer which is determined according to the equation from Jackson *et al.* (1996):

$$r_i = \left(\beta^{z_{h,j-1} \cdot 100} - \beta^{z_{h,j} \cdot 100} \right) \tag{18}$$

Where $z_{h,j}$ is the depth (m) from the soil surface to the interface between layers j and $j+1$, the factor 100 converts from m to

230   cm, and β is a species-dependent root distribution parameter (Jackson et al. 1996). Then, the conductance between each soil layer j and the stem apoplasm (K_{soil_j-Sapo}) is determined as the result of two conductances in series, K_{R_jT} and the conductance from soil to root ($K_{soil_j-R_j}$):

$$K_{soil_j-SApo} = \frac{1}{\frac{1}{K_{R_j-SApo}} + \frac{1}{K_{soil_j-R_j}}} \tag{19}$$

The conductance of the soil to fine roots $K_{soil_j-R_j}$ for each soil layer j is computed as:

$$K_{soil_j-Rj} = \frac{2\pi L_{a,j}}{ln\left(\frac{1}{r\sqrt{\pi L_{v,j}}}\right)} k_{sat} REW_j \left[1 - (1 - REW_j^{\frac{1}{m}})^m \right]^2 \tag{20}$$

with L_a and L_v the root length per soil area and soil volume for each soil layer respectively, and are computed from soil depth

235   and RAI_j whereas r is the radius of fine absorbing roots. k_{sat} is the soil hydraulic conductivity at saturation, m is a parameter of shape from the Van-Genuchten equation and REW is the relative extractable water content computed as:

$$REW = \frac{\theta - \theta_r}{\theta_s - \theta_r} \tag{21}$$

With θ the relative water content (soil water content per unit soil volume) changing dynamically with changes in absolute soil water reserve in the rooting zone, θ_s is the relative soil water content at saturation and θ_r is the relative soil water content at wilting point. θ_s and θ_r are parameters measured in the laboratory or derived from soil surveys with pedotransfer functions.

2.3.2 Cavitation

SurEau-Ecos also considers the capacitive effect of cavitation (Hölttä et al., 2009), i.e., the water released to the streamflow when cavitation occurs. The non-cavitated part of the xylem receives a water flux from the cavitated part, corresponding to F_L^{cav} in Eq. 6 ($F_L^{cav} > 0$), and then transferred to adjacent compartments. The amount of water corresponding to a new cavitation event is derived from the quantity of water in the apoplasm at saturation (Q_{LApo}^{Sat}) and the temporal variations in PLC_L such as:

$$F_L^{cav} = Q_{LApo}^{Sat} \max\left(\frac{dPLC_L}{dt}, 0\right)$$

(22)

This flux is linearized in temporal variations in ψ_{LApo} in order to express this flux in the form of a Darcy's law to match the generic form of equation 2. For that purpose, we introduce an equivalent conductance (K_L^{cav}) such as:

$$F_L^{cav} = Q_{LApo}^{Sat} \frac{dPLC}{d\psi} \frac{d\psi}{dt} \approx K_L^{cav} max\left(0, \psi_{LApo}^{cav} - \psi_{LApo}\right)$$

(23)

With $K_L^{cav} = -\frac{Q_{LApo}^{Sat} PLC'(\psi_{LApo})}{dt}$, PLC' the derivative of the PLC with respect to ψ which is computed from cavitation curve and ψ_{LApo}^{cav} the minimal value of potential ever reached over time, which controls the current cavitation level ($PLC_L = PLC_L(\psi_{LApo}^{cav})$). PLC' is computed as:

$$PLC' = -\frac{slope}{25} \frac{PLC}{100}\left(1 - \frac{PLC}{100}\right)$$

(24)

Following the same approach, the flux derived from the stem when cavitation occurs is defined as:

$$F_S^{cav} = Q_{SApo}^{Sat} \frac{dPLC_S}{dt} \approx K_T^{cav} max\left(0, \psi_{SApo}^{cav} - \psi_{SApo}\right)$$

(25)

2.4 Sources and Sink

2.4.1 Stomatal and cuticular plant transpiration

Plant loses water through stomatal transpiration (E_{stom}), cuticular transpiration of the leaf (E_{cuti_S}) and cuticular transpiration of the stem (E_{cuti_S}). Cuticular transpiration of the roots is considered to be negligible and is not taken into account. The total plant transpiration E_{Plant} is decomposed as the sum of the leaf (E_{leaf}) and wood transpiration (E_{cuti_S}):

$$E_{Plant} = E_L + E_{cuti_S}$$

(26)

Where E_{leaf} is computed as:

$$E_L = E_{stom} + E_{cuti_L} = \frac{1}{\frac{1}{g_{stom} + g_{cuti_L}} + \frac{1}{g_{bound}} + \frac{1}{g_{crown}}} \cdot \frac{VPD_{leaf}}{P_{atm}}$$

(27)

And E_{cuti_S} is computed as:

$$E_{cuti_S} = \frac{1}{\frac{1}{g_{cuti_S}} + \frac{1}{g_{bound}} + \frac{1}{g_{crown}}} \frac{VPD_S}{P_{atm}} \tag{28}$$

With $VPD_L (MPa)$ the vapor pressure deficit of the leaf, P_{atm} the atmospheric pressure (MPa), g_{stom} the stomatal conductance, g_{cuti_L} the cuticular conductance of the leaf, g_{bound} the conductance of the leaf boundary layer and g_{crown} the conductance of the tree crown.

VPD_L is a function of leaf temperature (T_L). T_L is computed at the leaf surface by solving the energy budget as in CPRM21. g_{bound} and g_{crown} are computed following Jones, (2013). g_{bound} varies with leaf shape, size (d_{leaf}) and wind speed; g_{crown} is a function of wind speed.

g_{cuti_L} is a function of T_L which is based on a single or double Q_{10} equation depending on whether leaf temperature (T_L) is above or below the transition phase temperature (T_{Phase}) (Cochard, 2019):

$$if\ T_L \le T_{phase}\ \ g_{cuti_L} = g_{\text{cuti20}_L} Q_{10a}^{\frac{T_L - 20}{10}} \tag{29}$$

$$if\ T_L > T_{phase}\ \ g_{cuti_L} = g_{\text{cuti20}_L} Q_{10a}^{\frac{T_{phase} - 20}{10}} Q_{10b}^{\frac{T_L - T_{phase}}{10}} \tag{30}$$

Where g_{stom} is the stomatal conductance taking into account the dependence of g_{stom} to light, temperature, and CO$_2$ concentration on the one hand, and water status on the other such as:

$$g_{stom} = \gamma \cdot g_{stom,max} \tag{31}$$

$g_{stom,max}$ is the stomatal conductance without water stress and is determined as a function of light, temperature and CO$_2$ concentration following Jarvis (1976). γ is a regulation factor that varies between 0 and 1 to represent stomatal closure according to ψ_{LSym} and an empirical sigmoid function depending on the potential at 50 % of stomatal closure ($\psi_{gs,50}$) and a shape parameter ($slope_{gs}$) describing the rate of decrease in stomatal conductance per unit water potential drop.

$$\gamma = 1 - \frac{1}{1 + e^{\frac{slope}{25}(\psi_{LSym} - \psi_{gs50})}} \tag{32}$$

2.4.1 Soil evaporation

E_{soil} is computed as the minimum of two supply function that both depend on maximum soil conductance (g_{soil0}) and the REW of the first soil layer such as

$$E_{soil} = min(g_{soil0} . REW_1 . \frac{VDP}{P_{Atm}}, g_{soil0} . REW_1 . (PET . e^{-k.LAI})) \tag{33}$$

Where the fraction of radiative energy (Potential evapotranspiration, PET) reaching the soil depends on the light extinction coefficient (k).

2.5. Capacitances

As described in Sect. 2.1, the link between Q and ψ are not represented in the same way for the soil and plant compartments. The notion of capacitance is used for the plant while water retention curves are used for the soil.

2.5.1. Plant compartments

The contribution of capacitance (C) to the plant compartment water balance is related to the saturated (or initial) water quantity (Q) in that compartment. Symplasmic and apoplasmic capacitances are not modelled in the same way but both require the water volume at saturation (Q^{sat}) of the considered reservoir. For the leaves, the volume of symplasmic and apoplasmic reservoirs at saturation (Q^{Sat}_{LSym} and Q^{Sat}_{LApo}, respectively) are defined as:

$$Q^{Sat}_{LSym} = (1 - \alpha_{LApo})Q^{Sat}_L \tag{34}$$

$$Q^{Sat}_{LApo} = \alpha_{LApo}Q^{Sat}_L \tag{35}$$

$$with\ Q^{Sat}_L = \frac{1}{LDMC - 1}DM = succulence \tag{36}$$

where DM is the dry matter per unit leaf area and the leaf dry matter content (LDMC), fraction of apoplasmic tissue in the leave (α_{LApo}) and leaf mass per area (LMA) are all input parameters.

The apoplasmic and symplasmic water quantities of the stem at saturation (Q^{Sat}_{SSym} and Q^{Sat}_{SApo}, respectively) includes the volume includes the roots, trunk and branches. They are computed based on the volume of the woody compartment and the water fraction of this volume such as:

$$Q^{Sat}_{SSym} = \frac{V_S}{M_{H_2O}} . \alpha_{Water} . \alpha_{SSym} \tag{37}$$

$$Q^{Sat}_{SApo} = \frac{V_S}{M_{H_2O}} . \alpha_{Water} . \alpha_{SApo} \tag{38}$$

Where V_S is the volume of tissue of the stem compartment (including the root, trunk and branches), M_{H_2O} is the water molar mass, α_{Water} is the proportion of water in this volume and α_{SApo} and α_{SSym} are the apoplasmic and symplasmic fraction of this water volume, respectively.

Symplasmic reservoirs behave as variable plant capacitances related to the pressure volume curve, which corresponds to the water quantity changes in symplasmic cells ($\frac{dQ}{dt}$). Symplasmic conductances are functions of the Q^{Sat}_{LSym} and the temporal change in the symplasmic relative water content (RWC) (illustrated here for the leaf but similar equations apply for the trunk):

$$\frac{dQ}{dt} = Q^{Sat}_{LSym}\frac{dRWC}{dt} = Q^{Sat}_{LSym}\frac{dRWC}{d\psi_{LSym}}\frac{d\psi_{LSym}}{dt} = C_{LSym}\frac{d\psi_{LSym}}{dt} \tag{39}$$

With this formulation the capacitance of the leaf symplasm (C_{Lsym}) can be written as:

14

$$C_{Lsym} = Q_{LSym}^{Sat} RWC' \qquad (40)$$

Where RWC' the derivative of the RWC with respect to ψ_{LSym}, derived from pressure-volume curves (Bartlett et al., 2012; Tyree and Hammel, 1972):

$$\psi_{LSym} = \begin{cases} -\pi_0 - \epsilon(1 - RWC) + \dfrac{\pi_0}{RWC}, & RWC \geq \dfrac{\pi_0}{\epsilon} + 1 \\[2mm] \dfrac{\pi_0}{RWC}, & RWC \leq \dfrac{\pi_0}{\epsilon} + 1 \end{cases} \qquad (41)$$

We used the following formulation for RWC' (see justification below for the expression above ψ_{tlp}):

$$RWC' = \begin{cases} \dfrac{RWC}{-\pi_0 - \psi_{LSym} - \epsilon + 2\epsilon RWC}, & \psi_{LSym} \geq \psi_{tlp} = \dfrac{1}{\dfrac{1}{\epsilon} + \dfrac{1}{\pi_0}} \\[4mm] -\dfrac{\pi_0}{{\psi_{LSym}}^2}, & \psi_{LSym} < \psi_{tlp} \end{cases} \qquad (42)$$

305 With

$$RWC = \frac{\pi_0 + \epsilon + \psi_{LSym} + \sqrt{\left(\pi_0 + \epsilon + \psi_{LSym}\right)^2 - 4\epsilon\pi_0}}{2\epsilon} \qquad (43)$$

When $\psi_{Lsym} \geq \psi_{tlp} = \dfrac{1}{\frac{1}{\epsilon} + \frac{1}{\pi_0}}$

In the above equation the formulation for $\psi_{LSym} < \psi_{tlp}$ simply results from the fact that $RWC = \dfrac{\pi_0}{\psi_{LSym}}$.

The case $\psi_{LSym} \geq \psi_{tlp}$ was obtained from basic manipulations of the derivation of the following form of the pressure volume curve:

$$\psi_{LApo}RWC + \pi_0 RWC + \epsilon(1 - RWC)RWC - \pi_0 = 0 \qquad (44)$$

310 Which derivative with respect to ψ_{LSym} is:

$$\psi_{LSym}RWC' + RWC + \pi_0 RWC' + \epsilon(1 - RWC)RWC' - \epsilon RWC RWC' = 0 \qquad (45)$$

So that $RWC' = \dfrac{RWC}{-\pi_0 - \psi_{LApo} - \epsilon + 2\epsilon RWC}$

Apoplasmic capacitance are constant and are computed as the product between Q_{Apo}^{Sat} and the specific apoplasmic capacitance (C_{Apo}). Note that given the very low elasticity of the xylem, their contribution is very weak.

2.5.2 Soil compartments

315 Capacitances for soil are not explicitly computed in *SurEau-Ecos*. Rather, soil water potentials for the different soil layers (ψ_{soil}, MPa) are directly computed according to the Van Genuchten parametric formulation (van Genuchten, 1980):

$$\psi_{soil} = \frac{\left(\left(\frac{1}{REW}\right)^{\frac{1}{m}} - 1\right)^{\frac{1}{n}}}{\alpha} \tag{46}$$

where m, n and α are empirical parameters describing the typical sigmoidal shape of the function and REW is the relative extractable water (see equation 21)

2.6. Numerical resolution

320 **2.6.1. Plant compartments**

The resolution of the plant hydraulic part of *SurEau-Ecos* is to solve the water balance for the four hydraulic compartments (i.e., nodes in Fig. 1c) whose equation are presented in Sect. 2.2.1. Three different numerical resolution schemes were implemented to solve water balances of plant compartments. For these three schemes, water potentials were discretized between two consecutive time steps ψ^n and ψ^{n+1}, separated by dt. Thanks to cautious hypotheses, these equations were

325 linearized at the first order in ψ, to lead to a four-equations linear system. In particular, we neglected all variations of capacitances and conductances during a given time step ($C \approx C^n$ *and* $K \approx K^n$), as these variations are expected to be marginal, with respect to weather changes, stomatal regulation or water release by cavitation.

The simpler *"explicit scheme"*, also implemented in *SurEau*, assumes that water fluxes can be expressed from the current time step *n* (see appendix B1 for details). From the generic water balance Eq. 4, it leads to:

$$C \frac{\psi^{n+1} - \psi^n}{dt} + \sum_j K_j\left(\psi^n - \psi_j^n\right) + S^n = 0 \tag{47}$$

330 Rearranging this equation, the potential at the next time step ψ^{n+1} can be simply computed as:

$$\psi^{n+1} = \psi^n + \frac{dt}{C}\left(\sum_j K_j\left(\psi_j^n - \psi^n\right) - S^n\right) \tag{48}$$

While the implementation of the explicit time integration scheme is undoubtedly the most straightforward numerical solution, it suffers, however, from a well-known numerical constraint referred to as the CFL, which imposes very small-time steps (dt) to avoid numerical instabilities:

$$dt \leq \frac{C}{2 \, max(K_j)} \tag{49}$$

This constraint implies that the smaller the *C*, the smaller the *dt*. An intuitive interpretation of this limitation is that the time

335 step needs to be small enough to avoid water movements between not adjacent cells. This constraint is particularly strong in plant xylem that is inelastic (i.e., C is very small) such that apoplasmic compartments cannot absorb water fluxes from their adjacent compartments when the time step is too large. This typically imposes time steps smaller than 10 ms (CPRM21).

A common option to avoid these numerical instabilities is to use an *"implicit scheme"*, where fluxes are estimated from the values of ψ at time n+1 (ψ^{n+1}) such as:

$$C\frac{\psi^{n+1} - \psi^n}{dt} + \sum_j K_j\left(\psi^{n+1} - \psi_j^{n+1}\right) + S^n = 0 \tag{50}$$

340 This numerical scheme is unconditionally stable, meaning that an increase in dt will not induce numerical instabilities but might however induce a loss of numerical accuracy. One very important limitation of this scheme is that the equations of the different compartments now correspond to a system of four equations that are coupled. Such a system can be linearized (by pieces to account for thresholds such as cavitation) and solved. In general, it implies the inversion of the matrix of the linear system, but the resolution can also be done analytically when the equations are not too many, as it is the case with *SurEau-*

345 *Ecos* (see details Appendix B2).

An alternative scheme, based on a "*semi- implicit"* approach, has also been recently proposed to solve water balances in plant hydraulic models while overcoming the numerical instabilities associated with an explicit formulation (De Kauwe et al., 2020; Li et al., 2021; Tuzet et al., 2017; Xu et al., 2016). Although not usual in numerical resolution approaches, this scheme showed great performance and led to convergence in simulations with time steps on the order of 10 minutes (Xu et al., 2016).

350 This approach consists in solving the differential equation of each compartment assuming that ψ_j and S remain constant (respectively equals to ψ_j^n and S^n) such as:

$$C\frac{d\psi}{dt} + \sum_j K_j\left(\psi - \psi_j^n\right) + S^n = 0 \tag{51}$$

After linearization of the coefficient, this ordinary differential equation has the following solution:

$$\psi(u) = \psi^n e^{-\frac{\sum_j K}{C}u} + \left(1 - e^{-\frac{\sum_j K_j}{C}u}\right)\frac{\sum_j K_j\psi_j^n - S^n}{\sum_j K_j} \tag{52}$$

So that ψ^{n+1} can be estimated by its value at $u = dt$:

$$\psi^{n+1} = \psi(dt) \tag{53}$$

$$\text{Which implies that } \psi^{n+1} = \eta\psi^n + (1 - \eta)\tilde{\psi} \tag{54}$$

$$\text{With } \eta = e^{-\frac{\sum_j K_j}{C}dt} \tag{55}$$

$$\text{And } \tilde{\psi} = \frac{\sum_j K_j\psi_j^n - S^n}{\sum_j K_j} \tag{56}$$

One can notice here that $\tilde{\psi}$ is the steady state solution of the equation, typically valid when C=0 (Fully elastic media).

355 In practice, this formulation is equivalent to the corresponding numerical scheme (provided that dt is very small):

$$C\frac{\psi^{n+1} - \psi^n}{dt} + \sum_j K_j\left(\psi^{n+1} - \psi_j^n\right) + S^n = 0 \tag{57}$$

This formulation allows comparing this scheme to the explicit and implicit schemes proposed above. This scheme uses ψ^{n+1} as a value for ψ (so that it remains stable) and ψ_j^n as a value of ψ_j (so that the equations of the four compartments are

decoupled) and can be seen as an intermediate between the explicit and the implicit scheme. For that reason, it will be referred

to as *"semi-implicit"* (Appendix B3). In theory, the water fluxes computed from values of water potentials evaluated at

360   different time steps should be less accurate than the implicit scheme, especially when water potential changes are fast. It is

thus expected that simulations require a larger time step to converge than the implicit scheme.

For the three different numerical schemes, we assume that soil potentials were estimated at the current time step n (i.e., $\psi_{S_j} \approx$

$\psi_{S_j}^n$) as in the explicit formulation (instead of $n+1$, as normally expected in an implicit scheme). This assumption is supported

by the very small variations in soil potentials occurring during a single time and avoids the linearization of soil potential

365   equations which would have required unnecessary complex developments.

Source and sink fluxes $S^{n+\frac{1}{2}}$ are computed for the climate at the middle of the time step (mid climate between current and next

time step, at $n + \frac{1}{2}$). For the implicit scheme, to account for the quick adjustment of stomatal regulation to climate variations,

$E^{n+\frac{1}{2}}$ accounts linear variations in water potential ψ_{LSym} over the time step, thanks to the derivative of transpiration function

$S'^{n+\frac{1}{2}}(\psi_{LSym}^n)$, also estimated for the mid climate, but current regulation ψ_{LSym}^n:

$$S^{n+\frac{1}{2}}\left(\psi_{LSym}^{n+\frac{1}{2}}\right) \approx S^{n+\frac{1}{2}}(\psi_{LSym}^n) + S'^{n+\frac{1}{2}}(\psi_{LSym}^n)\left(\frac{\psi_{LSym}^{n+1} - \psi_{LSym}^n}{2}\right)$$

$$= S^{n+\frac{1}{2}} + \frac{S'^{n+\frac{1}{2}}}{2}\left(\psi_{LSym}^{n+1} - \psi_{LSym}^n\right)$$

(58)

2.6.2. Soil compartments

370

Soil water balance in *SurEau-Ecos* is solved for each soil layer (Sect. 2.2.2) following a simple explicit scheme assuming that

water fluxes can be expressed from the current time step n. From the generic soil water balance Eq. 5, it leads to:

$$\frac{Q^{n+1} - Q^n}{dt} + K_{soil_j - SApo}(\psi_j^n - \psi_{SApo}^n) + S^n = 0$$

(59)

3. Impacts of numerical schemes on simulations and computation times

In this section, we explore the benefits and limitations of the three numerical schemes implemented in *SurEau-Ecos* to solve

375   water fluxes, namely an "explicit", "semi-implicit' and "implicit" scheme. As mentioned above, the minimal time step required

for accurate simulations is determined by computational limitations that depend on the chosen scheme. First, unlike the implicit

and semi-implicit scheme, the "explicit" scheme is limited by the CFL which causes numerical instabilities. We explored how

much computation time can be gained by using implicit or semi-implicit schemes compared to the explicit. In addition, in the

case of the implicit and semi-implicit scheme, reducing the temporal resolution (i.e., increasing the time step) can also limit

380   the accuracy of the simulation. The magnitude of corresponding errors then depends on the physiological processes at play in

the plant and on the precision of the numerical scheme. We also assessed the sensitivity of model outputs to the temporal resolution (time step *dt*) for the implicit and semi-implicit schemes.

For these simulations, all inputs were set identical to those used in the section dedicated to the evaluation of *SurEau-Ecos* (see Sect. 4). Daily weather was kept constant, without precipitation, and simulations were run until total hydraulic failure of the

385 plant. To compare the explicit scheme with the two other schemes, we made two slight simplifications to the model. First, we neglected the cavitation term in Eq.s 6 and 7. Indeed, the explicit numerical scheme of *SurEau-Ecos* cannot account for the flux term associated with water released by cavitation. This is due to the direct dependence of K_L^{cav} and K_S^{cav} to *dt* (Sect. 2.3.2) that prevents the CLF to be satisfied at any time step. Second, the values stem and leaf of apoplasmic capacitances (C_{SApo} and C_{LApo}) were increased (from about 1e^{-3} to 10 *mmol.m².MPa*) to decrease computational costs and ease the comparison between

390 the numerical schemes. The CFL constraint imposed very small-time steps (on the order of 1e-5 s) with the original values of plant apoplasmic capacitance, which caused unaffordable computation times under most CPUs. Preliminary analyses showed that the impact of C_{SApo} and C_{LApo} were negligible on simulation results for values up to 50-100 *mmol.m².MPa*.

When using the implicit or semi-implicit schemes with a relatively small-time step (*dt* =10s) our results show that these schemes yielded identical plant dynamics to those obtained with the explicit mode (Fig. 2). However, the gains in computation

395 time were considerable. Computation time was divided by about 10 for the implicit and semi-implicit scheme compared to the explicit scheme. This is because *dt* had to be set to 1s for the explicit theme because of the CFL. Any attempt to set a *dt* above this 1s threshold caused (as expected by the CFL) critical numerical instabilities (Fig. B1). Since some modifications to the model had to be performed for this comparison, the differences in computation times were solely indicative, reported to illustrate the benefits of the semi-implicit and implicit schemes compared to the explicit scheme. Our results showed that the

400 semi-implicit scheme was less accurate than the implicit scheme. Smaller time steps were required for the convergence of the model. Numerical explorations show that the semi-implicit scheme requires time steps on the order of 1 min (which is slightly slower than described in Xu *et al.* (2016) which stated that 10 minutes was enough), whereas the time step can be generally larger than 30 minutes with the implicit scheme (Figs. B2 and B3).

Resolution scheme	Time step	Computational time (s)
Explicit	1s	1403.98*
Implicit /Semi-implicit	10s	138.29
	1min	21.42
	Adaptative 'normal' (10-1min)	4.78
	10 min	3.35
	Adaptative 'fast' (60-10 min)	1.49

405

Tab. 2: Comparison of computation times between the three resolution schemes implemented in *SurEau-Ecos*. *This computational time is for indicative purposes only as several changes had to be made to the model to run it with the "explicit" scheme (see details in main text).

410 For the implicit and semi-implicit schemes, two adaptive time steps were further implemented to reduce computation times. This improvement was based upon the assumption that smaller time steps were only required when changes in two critical processes, stomatal regulation and cavitation, were the highest. In a *"Normal"* mode, the base time step is at 10 minutes but is automatically and gradually refined up to 1 min in periods of intense regulation changes, based on a criterion aiming at preventing variation in stomatal regulation and cavitation of more than 1% between two consecutive time steps. In a *"Fast"*

415 mode, the base time step is at 1h refined up to 10 minutes. The implementation of adaptative time steps allowed to further increase this gain in computing time (Tab. 2) without affecting plant dynamics.
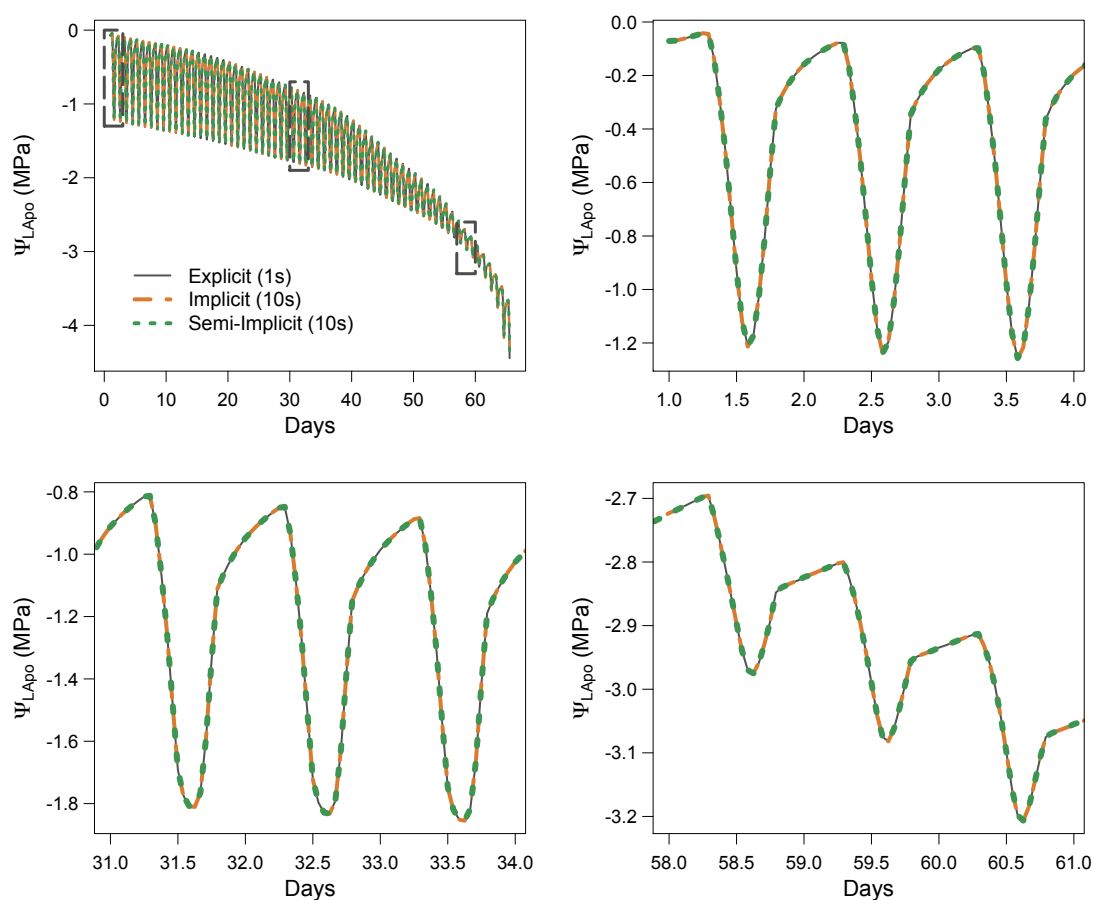

Fig. 2: Comparison of the three numerical schemes implemented in *SurEau-Ecos* to solve water balances. Computation times for each scheme are given in Tab. 2.

420

4. Comparison between *SurEau-Ecos* and *SurEau*

SurEau-Ecos relies on the same biological and physical principles of *SurEau* (CPRM21). The soil-plant-atmosphere system is segmented and described as compartments linked together and exchanging water fluxes according to the gradients of water potential and hydraulic conductances. However, significant disparities between the implementation, parametrization, and

425 resolution of water fluxes between the two models lead to some major differences in plant architecture and representation of water fluxes. It was therefore essential to confirm that both models provide comparable dynamics of the main state variables under similar conditions. This comparison of model outputs also consists at as an indirect validation effort of *SurEau-Ecos* since *SurEau* has been validated against field data (see details in CPRM21).

We identified three major differences in plant architecture and representation of hydraulic processes within the models. First

430 plant architecture is simpler in *SurEau-Ecos* than in SurEau. *SurEau-Ecos* represents the plant as two leaf cells (leaf apoplasm and leaf symplasm) and two stem compartments that include the woody volume of branches, trunk and root. By contrast, *SurEau* offers a detailed plant organ discretization (including roots, trunk, branches, leaves and buds). Second, while both models represent the belowground stems by three roots in parallel, the resistance to water flow linked to the root endoderm (a symplasmic root resistance) is not explicitly included in *SurEau-Ecos* contrary to *SurEau*. Instead, only one resistance per

435 root, from the root entry to the stem is accounted to mimic all possible resistance (root symplasm and apoplasm). Finally, in *SurEau-Ecos,* all leaf level fluxes to the atmosphere -- i.e., the stomatal and the cuticular fluxes -- pass through the symplasm, whereas in *SurEau* stomatal fluxes pass through the apoplasm and cuticular fluxes.

To compare model outputs, we performed an equivalent parameterization of the two models (see details in Fig. B4) and ran simulations until total hydraulic failure of the plant. We started the comparison with a typical plant fully described in CPRM21

440 whose parameters are given for each organ in Tab. B2. We then aggregated the values of *SurEau* parameters to match the following input parameters of *SurEau-Ecos*: water quantities of the leaf and stem compartments (Q_{LApo}^{sat}, Q_{LSym}^{sat}, Q_{SApo}^{sat} and Q_{SSym}^{sat}), the symplasmic conductance of the stem (K_{SSym}), the apoplasmic root to stem conductance (K_{R-SApo}) and the apoplasmic stem to leaf conductance ($K_{SApo-LApo}$). We also set the cuticular conductance of non-leaf organ to 0 in both models. All other sub models, parameters and environmental forcing (weather and soil) were also set equal including stomatal,

445 boundary layer and crown conductance, linear approximation for the leaf energy balance, soil parameters and hourly climatic inputs. This ensured that any divergence between models could only come from either the numerical scheme or plant hydraulic architecture.

Fig. 3 shows the dynamics of water potentials, leaf transpiration and percent loss of conductance obtained when simulations were run from a wet soil profile until hydraulic failure is reached. Note that for this comparison the output of the trunk in

450 *SurEau* were compared to the stem in *SurEau-Ecos*. For both models, at the beginning of the simulations, when the soil was wet, leaf and stem water potentials followed the hourly variations in meteorological conditions, thereby reflecting the response of stomata to light and response of plant transpiration to g_{stom} and VPD. As soil reservoir emptied, stomata progressively closed according to the intensity of foliar water potential. After about 65 days for both models, the stomata permanently closed

and transpiration was limited to cuticular losses which gradually accentuated the drought stress of the plant (decreased plant
455 water potentials). Simultaneously, cavitation increased in the different organs, inducing water release from the apoplasm which
partly dampened the decrease in plant water potentials. These results show that *SurEau-Ecos* and *SurEau* yielded very similar
results when parametrized in such a way that plant organs had by similar conductances and water reservoirs.

Despite similar dynamics, we also identified some differences in infra daily water potentials between the two models. As a
result, the time to leaf hydraulic failure was underestimated by three days (out of 90 days) in *SurEau-Ecos* compared to *SurEau*.
460 These slight differences can be linked to the presence of the higher number of compartments in *SurEau* that increase the
seasonal dampening effect of water potential compared to SurEau-Ecos where in a lower number of compartments are
represented. Notably, we observed some differences between the short-term (infra daily) variations of water potential dynamic
of the trunk symplasmic compartment of *SurEau* and the stem compartment of *SurEau-Ecos* (that includes the volume of roots,
trunk and branches, Tab. B2). The daily magnitude of the fluctuation in *SurEau-Ecos* appeared more dampened (Fig. 3, Figs
465 B5 and B6). The most plausible explanation for this difference is that the volume of the stem compartment in *SurEau-Ecos* is
greater than the volume of the trunk compartment in *SurEau*. This is likely to lead to greater water discharge and lower water
potential fluctuations in *SurEau-Ecos* (Fig. B6). Ongoing developments of a modular version of *SurEau* within the *Capsis*
modeling platform (Dufour-Kowalski et al., 2012) will allow to evaluate more deeply the effects of plant hydraulic architecture
on the dynamics of plant desiccation.
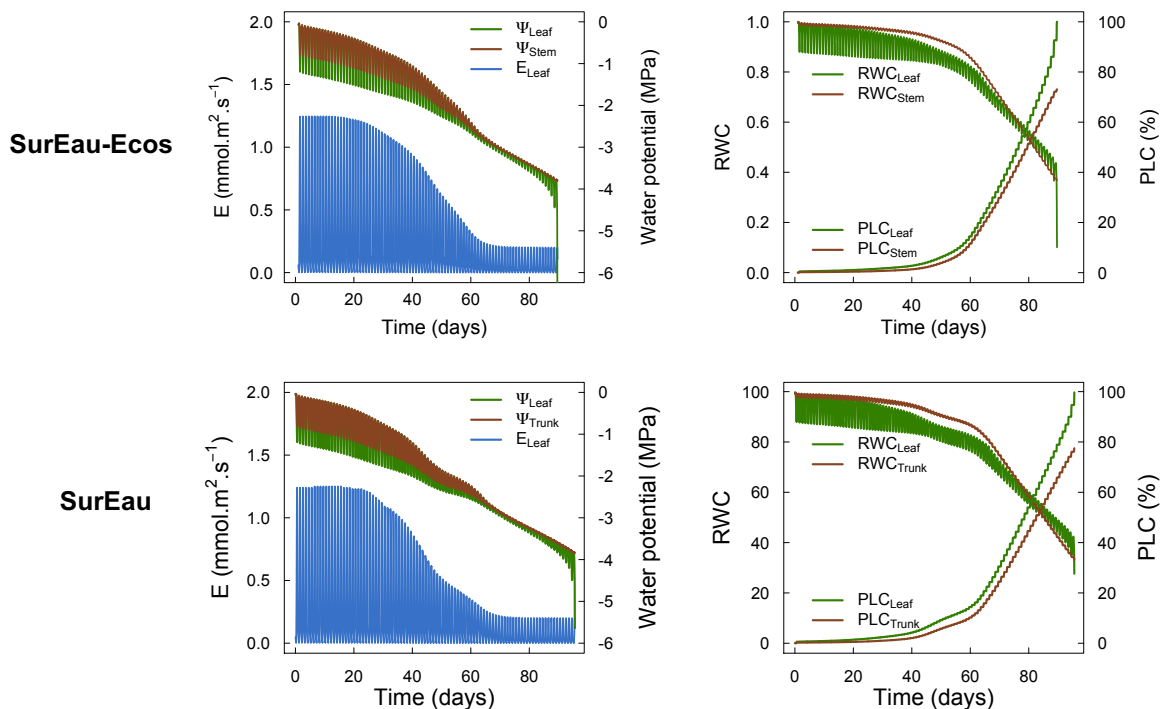
470

Fig. 3. Comparison of the dynamics of plant water status between *SurEau-Ecos* and *SurEau*.

5. Sensitivity analyses of drought-induced tree mortality to input parameters

We carried out a variance-based sensitivity analysis to gain insight into the hydraulic traits and stand parameters that influence plant dynamics in *SurEau-Ecos* and to explore the main drivers of tree resilience to extreme drought. Variance-based

475 approaches can measure sensitivity across the whole input space (i.e., it is a global method) and quantify the effect of interactions that can be unnoticed on a local sensitivity analysis approach (i.e., when moving one parameter at a time). Here, we used the Sobol' sensitivity analysis method (Sobol, 2001) and reported 'total order indices' that quantify the contribution of each parameter to the variance of the model output.

Two different physiological phases control the dynamics of plant desiccation under extreme drought, according to whether

480 ψ_{LSym} is above or below the point of stomatal closure (Fig. 1a). Three time-based metrics were, therefore, considered to explore the sensitivity of plant desiccation to input parameters: (i) the time to hydraulic failure, (ii) the time to stomatal closure, and (iii) the survival time, defined as the time difference between hydraulic failure and stomatal closure (see an illustration of these metrics in Fig. 4). We performed a sensitivity analysis for three different tree species with contrasted ecology and exhibiting various combinations of input parameters (Tab. 3). For each parameter, we randomly sampled a value within a range of $\pm 20\%$

485 of the observed value. Starting from a wet soil, and without further precipitation, we ran simulations until hydraulic failure of the plant, defined as the moment when leaves reach 99 % loss of hydraulic conductivity (PLC_L>=99 %). This threshold guarantees that plant water pools were almost empty and that no other water reservoirs are available for the plant. Daily climate inputs were set constant according to the simulations shown in Sect. 4. In total, we ran 700,000 simulations in the sensitivity experiment

490 We based our selection of stand, plant and soil parameters used in the sensitivity analysis on the results from preliminary analyses and from findings by CPRM21. For stand traits, we focused on LAI_{max}, canopy conductance (g_{canopy}) and total available water content available for the plant (TAW). TAW is not an input parameter in *SurEau-Ecos*, but it is an integrative index resulting from the interaction between soil characteristics and rooting depth. To make TAW vary in simulations without affecting soil physical properties, we adjusted rooting depth such as to match the targeted TAW. g_{canopy} is also not an input

495 parameter in *SurEau-Ecos* but also an integrative index resulting from the interactions between g_{bound}, g_{stom_max} and g_{crown0}. The following physiological and hydraulic traits were also included: P_{50}, $slope_{gs}$, $\psi_{gs,50}$, $slope_{gs}$, $k_{R-SApo,max}$, $k_{SApo-LApo,max}$ k_{SSym}, g_{cuti20}, Q_{10a} and Q_{10b}, π_0 and V_S (see definition in Tab. 1).

Our results showed that a few parameters explained most of the variability in the resilience of trees to extreme drought (Fig. 4) albeit their importance largely depended on the physiological phase under study. Variations in LAI_{max}, TAW, $\psi_{gs,50}$ and

500 g_{canopy} mainly explained the variance in time to stomatal closure, i.e., the first physiological phase. It suggests that, in this phase, interactions between how much water is available in the soil (TAW) and how fast plant transpiration will empty that reservoir (LAI_{max}, $\psi_{gs,50}$ and g_{canopy}) determine the time to stomatal closure. In the second phase (after stomatal closure), survival time was mostly driven by LAI, g_{min20}, Q_{10a}, P_{50}, TAW, and V_S. In that phase, the importance of stand parameters (LAI_{max} and TAW) decreased to the benefit of traits related to the rate of water losses through cuticular transpiration (g_{cuti20}

505   and Q_{10a},), the volume of water reservoirs in the root, trunk and branches (V_S) and plant resistance to cavitation (P_{50}). When both phases were considered jointly, we observed that the variability in the time to hydraulic failure was mainly associated with stand parameters (LAI and TAW) and to a lesser extent with $\psi_{gs,50}$ and g_{cuti20}.

We also observed that the patterns described here above were almost identical regardless of the vegetation type under study. In particular, the parameters controlling 'time to hydraulic failure' and 'survival time' were similar among the three studied

510   vegetation types, suggesting a similarity of plant adaptation strategies to avoid hydraulic failure in a changing climate. The one exception to this pattern is the importance of varying plant resistance to cavitation ($\psi_{50,L}$) in survival time. The influence of $\psi_{50,L}$ ranged from low for *Quercus ilex* (about 0.05) to very important for *Quercus Petraea* (about 0.37). This observation suggests that less drought-resistant species (with higher $\psi_{50,L}$) have a more direct benefit of lowering their ψ_{50L} to increase their survival time than drought-resistant species (with lower $\psi_{50,L}$). This might be due to the non-linear response of water

515   potential to soil and plant water content, which implies that the rate of change of plant water potential increases as soil and plant water content decreases.

24
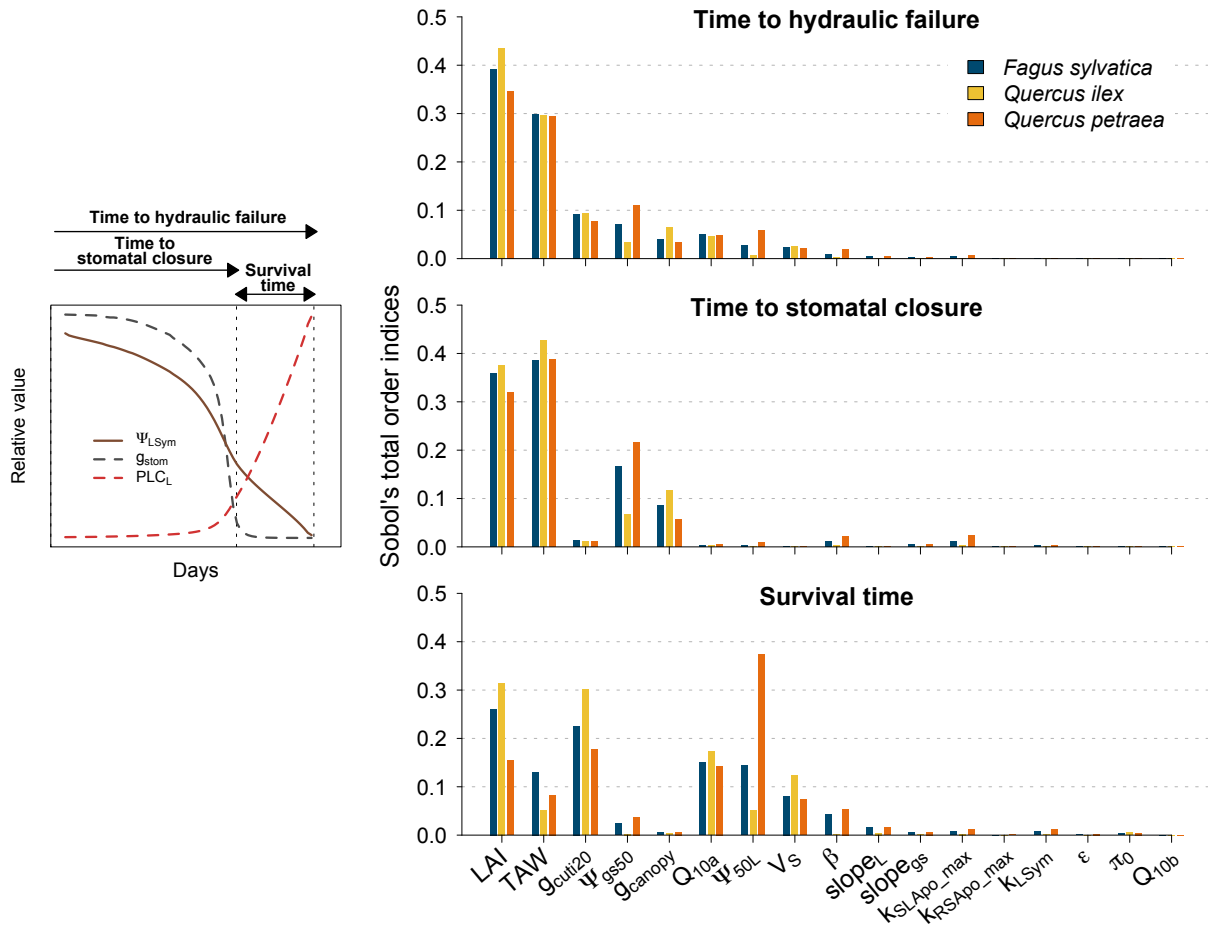
Fig. 4: Global sensitivity analysis of plant desiccation dynamics to the main hydraulic traits and stand parameters in *SurEau-Ecos*, shown for three different tree species with contrasted ecology and exhibiting various combinations of input parameters (see main input parameters in Tab. 3). We explored the sensitivity of three physiological time-based metrics to input parameters: time to stomatal closure, time to hydraulic failure, and survival time. These three metrics describe the two different physiological phases controlling the dynamics of plant desiccation under extreme drought, according to whether ψ_{LSym} is above or below the point of stomatal closure (Fig. 1a). All hydraulic and stand traits varied from +- 20 % around their original value. TAW is the total available water for the plant.

Our results shed some light on our understanding of plant functioning under extreme drought. We highlighted the prominent

530 role of stand traits, namely LAI and TAW, along with $\psi_{gs,50}$ in determining the time needed to reach stomatal closure. By contrast, physiological variables, namely g_{cuti20}, Q_{10a}, V_S and $\psi_{50,L}$ played a more important role in determining 'survival time'. Two improvements to the present analyses may strengthen these findings. First, numerous correlations exist between those traits, reflecting trade-offs and plant functioning strategies (Bartlett et al., 2012; Christoffersen et al., 2016) that we did not take into account. Second, the relative importance of input parameters is likely to be influenced by climate. For instance,

535 we would expect the influence of g_{min20}, Q_{10a} and Q_{10b} on survival time to increase when temperature increases, following previous results showing the vulnerability of trees during heatwaves (Cochard et al. 2020). Integrating these potential improvements in future simulations may further help elucidate the specific spatial and temporal patterns of drought-induced mortality (Meir et al., 2015).

Parameter	Quercus ilex	Fagus sylvatica	Quercus Petraea
LAI_{max}	3	5	6
ε_L	10	10	10
π_{0_L}	-2.1	-1.9	-2.1
$\psi_{gs,50}$	-2.8	-1.8	-2.34
$slope_{gs}$	44	130	92
g_{cuti20}	3	4	3
Q_{10a}	1.2	1.2	1.2
Q_{10b}	4.8	4.8	4.8
T_{Phase}	37.5	39	42
$\psi_{50,L}$	-7	-3.15	-3.4
$slope_L$	30	40	60
$K_{R-SApo,max}$	2.5	2.5	1.55
$K_{SApo-LApo,max}$	5	5	3.1
K_{SSym}	0.26	0.26	0.26
K_{LSym}	2.5	2.5	1.55
g_{stom_max}	200	200	200
β	0.97	0.98	0.97
V_S	20	33	40

540

Tab. 3. Main parameter's values used in model simulations whose results are shown in Figs. 4 and 5. Parameters derived from pressure-volume curves and PLC curve were set equal for the leaf and leaf ($\varepsilon_S = \varepsilon_L$, $\pi_{0_S} = \pi_{0_L}$, $slope_S = slope_L$, $\psi_{50,S} = \psi_{50,L}$).

6. Regional prediction of climate-change impacts on tree mortality

In this section, we aimed to illustrate the potentialities which *SurEau-Ecos* will provide to improve our understanding of forest
545 vulnerability to drought. We explored whether the probability of plant hydraulic failure simulated by *SurEau-Ecos* was related
to the distribution of two tree species across climate gradients and, then, to identify future areas at risk of drought-induced tree
mortality. Specifically, we hypothesized that hydraulic failure was a significant constraint to tree distribution at the regional
level.

We quantified the probability of hydraulic failure over France (544,000 km^2) for two different species chosen for their
550 contrasted functioning strategies: an evergreen Mediterranean Oak (*Quercus ilex*) and a temperate deciduous European Beech
(*Fagus sylvatica*) (see main parameters in Tab. 3). *Quercus ilex* is a drought-resistant species with low LAI, P$_{50}$, and deep-root
systems to extract water from cracks in the bedrocks during drought. By contrast, *Fagus Sylvatica* is characterized by a higher
vulnerability to drought (higher P$_{50}$) and higher LAI values. As in Sect. 5, we defined hydraulic failure as the point when leaves
reach 99 % loss of hydraulic conductivity (PLC_L>=99 %). For each period investigated, we reported the probability of hydraulic
555 failure as the frequency of years during which PLC_L>=99 %.

We ran simulations for present (1991-2020) and future (2071-2100) periods at an 8 km^2 resolution over France for both species.
Climate data for the present period (1970-2020) were extracted from the SAFRAN climate reanalysis database (Vidal et al.,
2010) that covers France at an 8 km^2 resolution. Projections of climate variables for the future climate period (2071-2100)
were obtained from a climate simulation program involved in the 5th phase of the Coupled Model Intercomparison Project
560 (CMIP5) and produced as part of the EURO-CORDEX initiative (Kotlarski et al., 2014). One single GCM-RCM couple was
extracted for these analyses (i.e., MPI-ESM-REMO2009), which was chosen because of its averaged climate trajectory over
France when compared to an ensemble of GCM-RCM couples (Fargeon et al., 2020; Ruffault et al., 2020). Data were extracted
at a 0.44° spatial resolution for the historical (1990–2005) and future (2006–2099) periods. Model outputs were bias-corrected
and downscaled at the 8 km^2 resolution using a quantile-quantile correction approach (Ruffault et al., 2014).

565 To apply the model at the landscape scale, we made several simplifying assumptions. First, we assumed that each 8 km^2 grid
cell was covered by trees of the same species and LAI was set to a constant value representative of observed values for the
considered species (Tab. 3). Second, soil characteristics were also set constant over the territory. Both assumptions are
unrealistic because stand characteristics vary at the local scale and have a primordial role in the probability of hydraulic failure
(Sect. 5). However, as we aimed to assess the regional (rather than the local) vulnerability of tree species to changes in climate,
570 we did not expect this to be a main limitation, provided that the results of these simulations be interpreted accordingly to these
assumptions. To assess whether the probability of hydraulic failure was a good proxy of the current southern range of tree
species distribution, we compared the results of our simulations with presence/absence data for each species. Tree species data
were extracted from the national forest inventory database (available at *http://www.ifn.fr*) and aggregated to obtain presence-
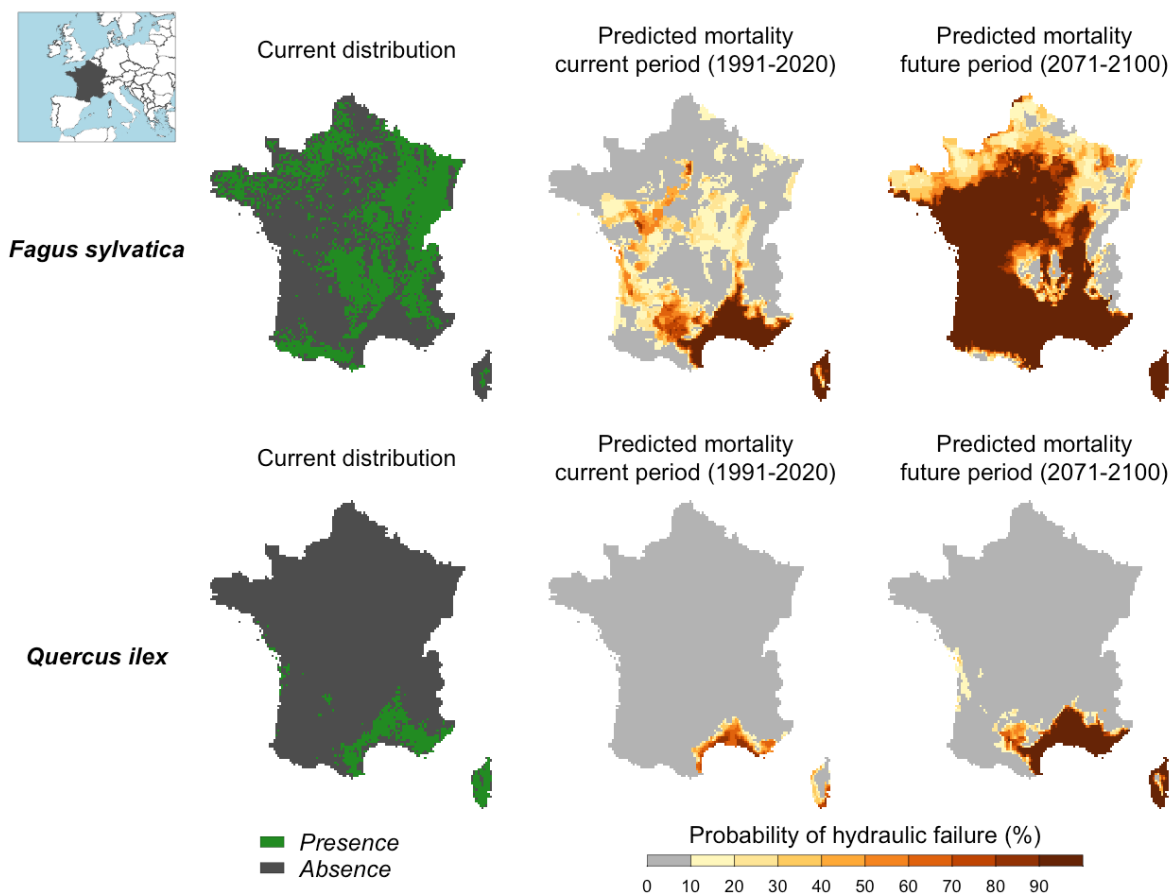absence on the 8-km studied grid, following Cheaib et al. (2012).

575   Maps of probability of hydraulic failure (probability of reaching PLC_L>=99 %) are shown in Figure 5. We observed contrasted regional patterns according to the species under study. We observed a higher probability of mortality in south-eastern France for both species but the probability of hydraulic failure was higher for the European Beech than for the holm oak. In the rest of the country, the probability of hydraulic failure was almost 0 for the holm oak. By contrast, we observed probabilities up to 50 % for the European beech in the western part and middle of the country, where the climate is temperate. When comparing

580   these results with the maps of current species distribution, we observed a reasonable degree of spatial agreement between our simulations and presence/absence data. European beech was predominantly present in areas where our simulations indicated a probability of drought-induced mortality equal to 0 %. However, we could not interpret the results for the holm oak in the same way since the current distribution of this species indicates that the southern climate margin is not reached in the present climate.

585   Our projections for the end of the century showed a future increase in the areas characterized by a high risk of hydraulic failure over France. For *Fagus Sylvatica* the areas characterized by a high risk of hydraulic failure will extent towards the northeast and west of the country over the major part of the territory. For *Quercus ilex*, our simulations indicated that the probability of hydraulic failure should significantly increase in the South-eastern France where this species is currently widespread. Altogether, these results indicate that future climate conditions might overcome the capacity of the two studied tree species to

590   face drought over the French territory, which might increase the likelihood of tree mortality and wildfires in the future. Adding information on LAI and soil physical properties might further refine our simulation results. LAI can be estimated from remote sensing indices (see for instance De Kauwe et al., 2020b). However, TAW estimations are more problematic because the information on root depth is rarely available (Ruffault et al., 2013; Venturas et al., 2020).

Fagus sylvatica

Current distribution

Predicted mortality
current period (1991-2020)

Predicted mortality
future period (2071-2100)

Quercus ilex

Current distribution

Predicted mortality
current period (1991-2020)

Predicted mortality
future period (2071-2100)

Presence
Absence

Probability of hydraulic failure (%)

0 10 20 30 40 50 60 70 80 90

Fig. 5: Probability of hydraulic failure (%) over the past (1991-2020) and future (20717-2100) period for two tree species in France simulated with *SurEau-Ecos*. The Current distribution is shown for comparison with the simulated risk of hydraulic failure.

7. Conclusion

Drought is arguably one of the most important natural disturbance threatening forest ecosystems in a number of regions worldwide (Anderegg et al. 2020). The challenges facing our understanding of the role of plant hydraulics in vegetation dynamics are numerous (McDowell et al., 2019), one being the ability of current vegetation models, including those based on plant hydraulics, to predict plant desiccation dynamics at regional scales (De Kauwe et al., 2020; Rowland et al., 2021; Trugman et al., 2021; Venturas et al., 2020). Here, we presented *SurEau-Ecos*, a new plant hydraulic SPA model aimed at predicting plant water status and drought-induced mortality at scales from stand to region. *SurEau-Ecos* was designed to simulates plant water status of the different plant's compartments, while balancing for the need of input parameters and computational requirements. *SurEau-Ecos* simulates key mechanisms associated with plant desiccation during drought and heatwaves, including the dynamics of plant's water status beyond the point of stomatal closure via residual transpiration flow,

plant cavitation and solicitation of plants' water reservoirs. We showed that *SurEau-Ecos* was able to provide accurate estimations of plant water status dynamics compared to the *SurEau* model, despite that this latter represents plant hydraulics mechanisms in more details. This confirms that, for large-scale applications, the changes we implemented in *SurEau-Ecos*

610 largely outweigh a potential loss of accuracy associated with the simplification of plant architecture and hydraulic processes. *SurEau-Ecos* provides the capability to better understand the role of plant-hydraulics in vegetation dynamics under climate change conditions characterized by increased drought frequency.

Appendix A: Leaf phenology module in *SurEau-Ecos*

Leaf area index (LAI) of the stand is updated daily. Species can have either evergreen or winter deciduous phenology.

615 Evergreen species are assumed to maintain a constant LAI throughout the year. LAI values of deciduous plants are adjusted as a function of leaf phenology ($\emptyset$) and the maximum of the stand (LAI_{max}) such as:

$$LAI = \emptyset \cdot LAI_{max} \qquad (A1)$$

$\emptyset$ is set to 0 until budburst occurs. Budburst is assumed to be driven by the cumulative effect of forcing temperatures (R_f) on bud development (Chuine and Cour, 1999) such as:

620 $$\sum_{t_0}^{t_f} R_f(T_d) \geq F* \qquad (A2)$$

Where t_0 is a parameter defining the initial date of the forcing period, t_f the budburst date and F* is a parameter defining the amount of forcing temperature to reach budburst. Once budburst, $\emptyset$ increases from 0 to 1 at a rate specified by a parameter describing the LAI growth rate per day (R_{LAI}). In autumn, leaf fall occurs ($\emptyset$ starts to decline) when the average daily temperature falls below 5ºC (De Cáceres et al., 2015; Sitch et al., 2003) and then $\emptyset$ declines at a similar rate to LAI growth in

625 spring.

Appendix B: additional tables and figures

Symbol	Unit	Description
T_{mean}	°C	Mean temperature
T_{min}	°C	Minimum temperature
T_{max}	°C	Maximum temperature
R_{global}	MJ.m^{-2}	Global radiation
ppt	mm	Precipitation
RH_{mean}	%	Mean relative humidity
RH_{min}	%	Minimum relative humidity
RH_{max}	%	Maximum relative humidity
u	m.s^{-1}	Mean wind speed

Tab. B1: Daily climate input variables.

630

SurEau "Trunk-only"					
	Parameters	**Leaf**	**Branches**	**Trunk**	**Root**
Symplasm	π_0 (MPa)	2.1	-2.1	-2.1	-2.1
	ϵ (MPa^{-1})	10	10	10	10
	K (mmol s^{-1} MPa^{-1}.m^{-2})	1.80	0.55	0.26	7.22
	$Qsat$ (mol.m^{-2})	43.75	91.12	355.73	377.77
	Surface (m^2)	10.5	5.8	2.7	54.1
Apoplasm	$P50$ (MPa)	-3.4	-3.4	-3.4	-3.4
	$Slope$ (% MPa^{-1})	60	60	60	60.
	K (mmol s^{-1} MPa^{-1}.m^{-2})	1.32	6.50	7.16	2.03
	$Qsat$ (mol/m^{-2})	14.58	182.25	711.46	658.8
SurEau-Ecos					
	Parameters	**Leaf**	**Stem**		
Symplasm	π_0 (MPa)	-2.1	-2.1		
	ϵ (MPa^{-1})	10	10		
	K (mmol s^{-1} MPa^{-1}.m^{-2})	1.80	0.84		
	$Qsat$ (mol.m^{-2})	4.16	78.53		
	Surface (m^2)	10.5	62.6 (All wood)		
Apoplasm	$P50$ (MPa)	-3.4	-3.4		
	$Slope$ (% MPa^{-1})	60	60		
	K (mmol s^{-1} MPa^{-1}.m^{-2})	1.32	3.4		
	$Qsat$ (mol/m^{-2})	1.4	148		

Tab. B2 Main physiological parameters of plant compartments used for the comparison between *SurEau* and *SurEau-Ecos*.
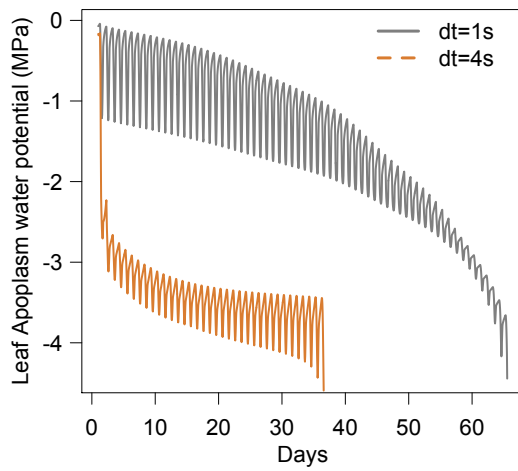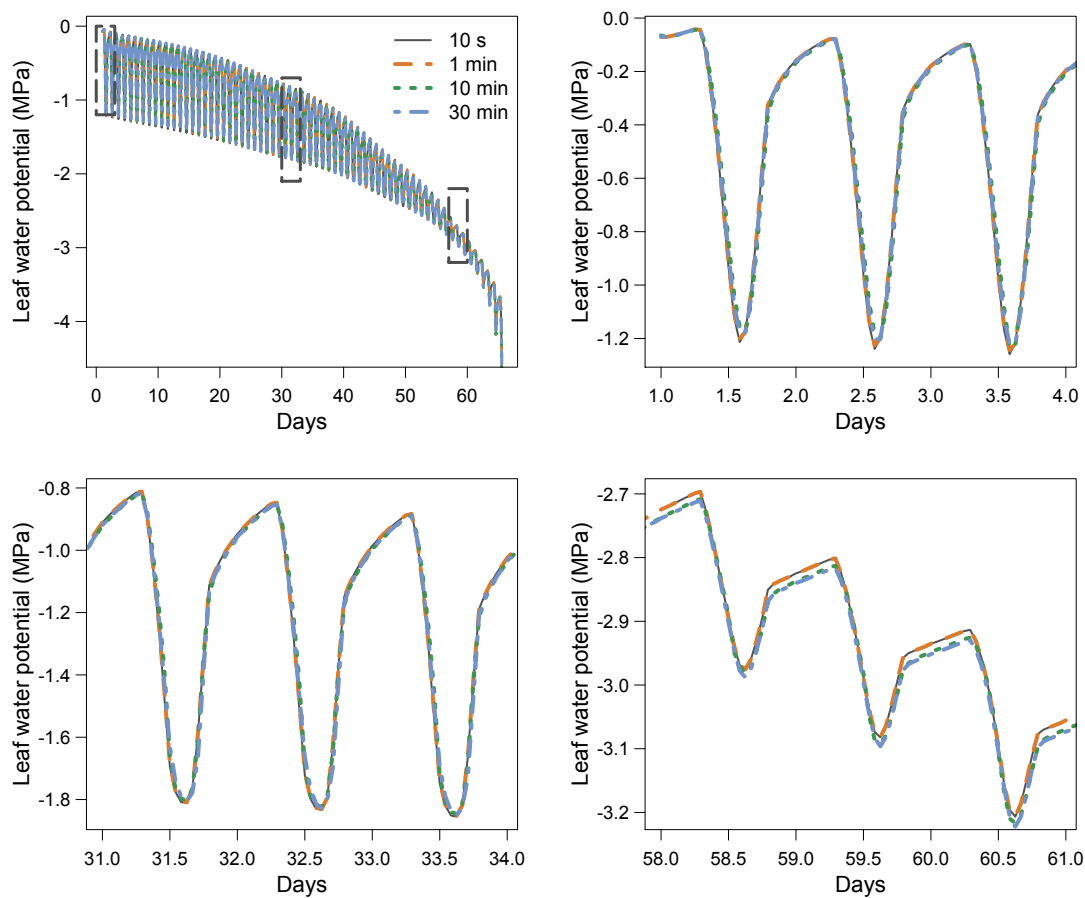
635

Fig. B1: Illustration of the constraint on *dt* due to the Courant–Friedrichs–Lewy (CFL) condition in *SurEau-Ecos*. When dt > 2*K/C numerical instabilities are observed.

640 **Fig. B2: Impact of the time step (dt) on simulation results with the 'implicit' resolution scheme.**
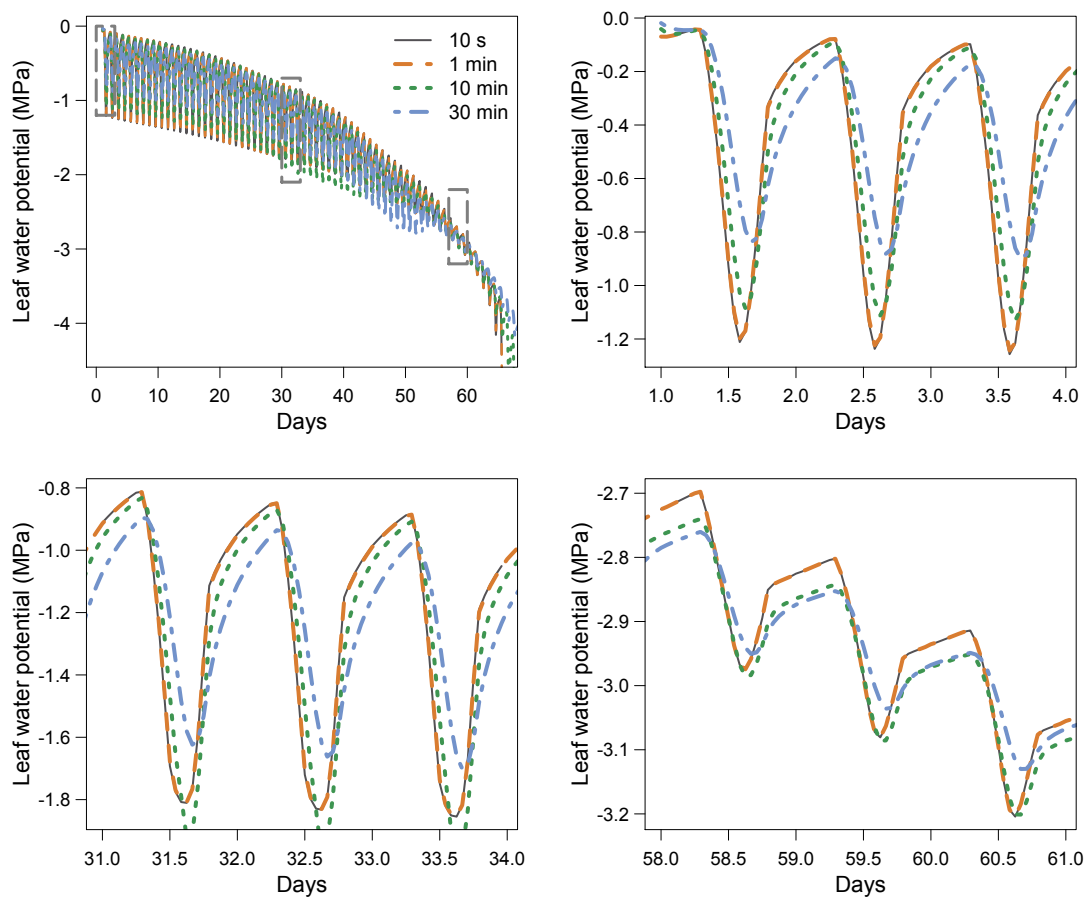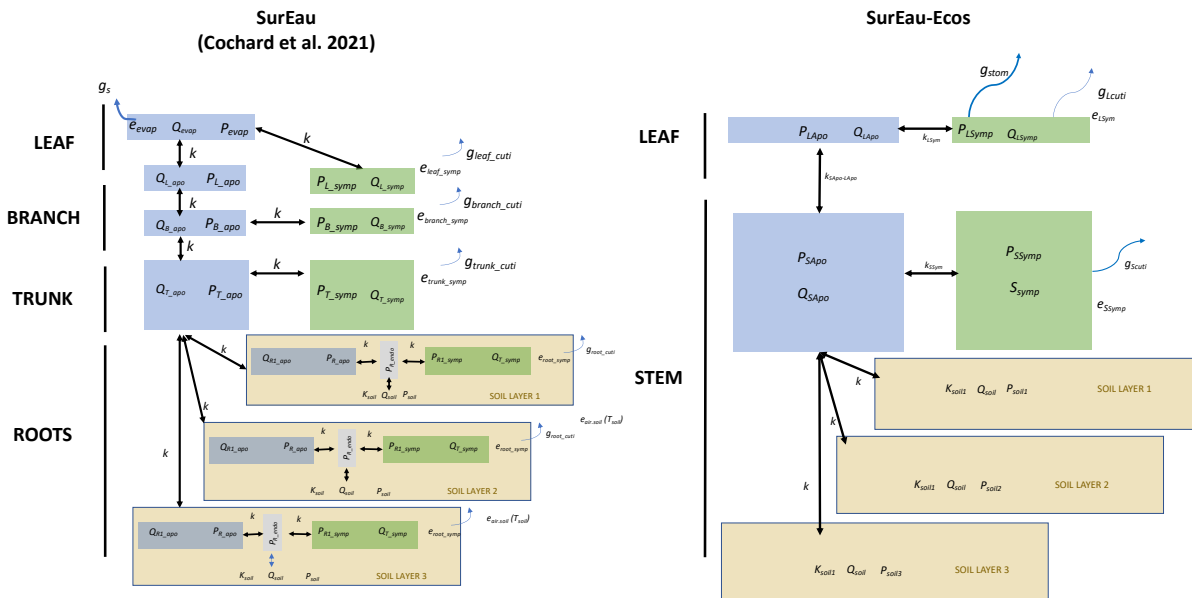
Fig. B3: Impact of the time step (dt) on simulation results with the 'semi-implicit' resolution scheme.

645

Fig. B4: Comparison of the plant architecture in *SurEau* and *SurEau-Ecos*. Q indicates the water quantities of the compartments, P the water potentials, k the hydraulic conductances, gs the gaseous stomatal conductances and g_cuti the gaseous cuticular conductances. The subscripts *Apo*, *Sym* and *Endo* indicate the apoplasm, symplasm and endoderm compartments, respectively. The subscripts L, S, B, T, and evap stand for Leaf, Stem, Branch, Trunk, Root and Evaporative site respectively
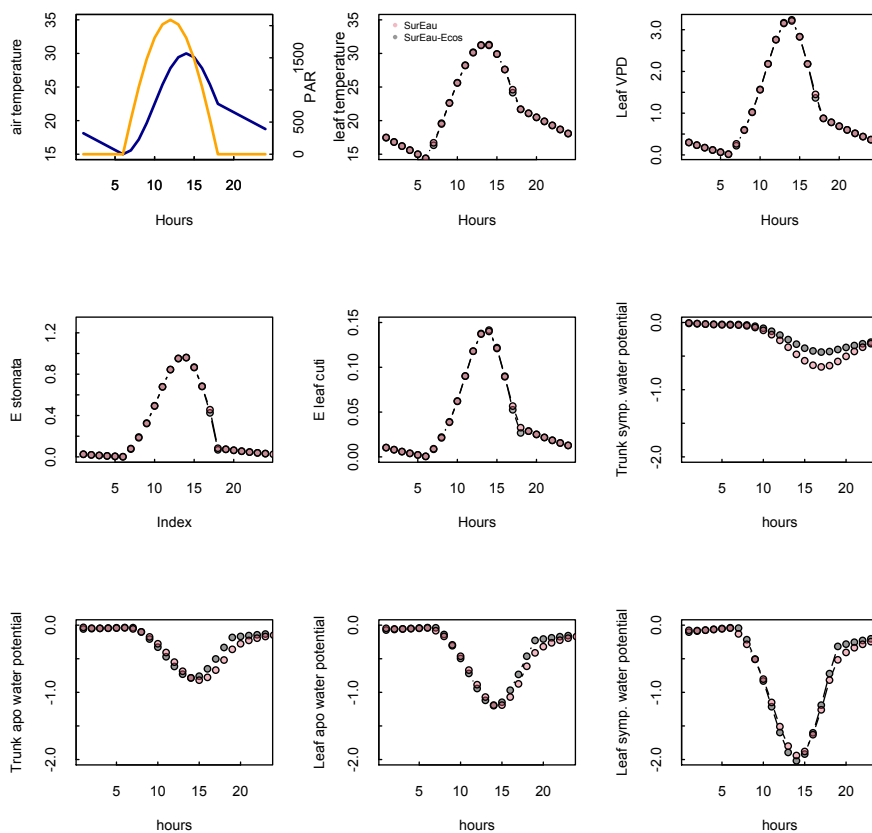
Fig. B5: Comparison of hourly outputs between *SurEau* and *SurEau-Ecos* for the first day of simulation. Climatic inputs (Radiation, temperature and VPD) are shown in the first panel.
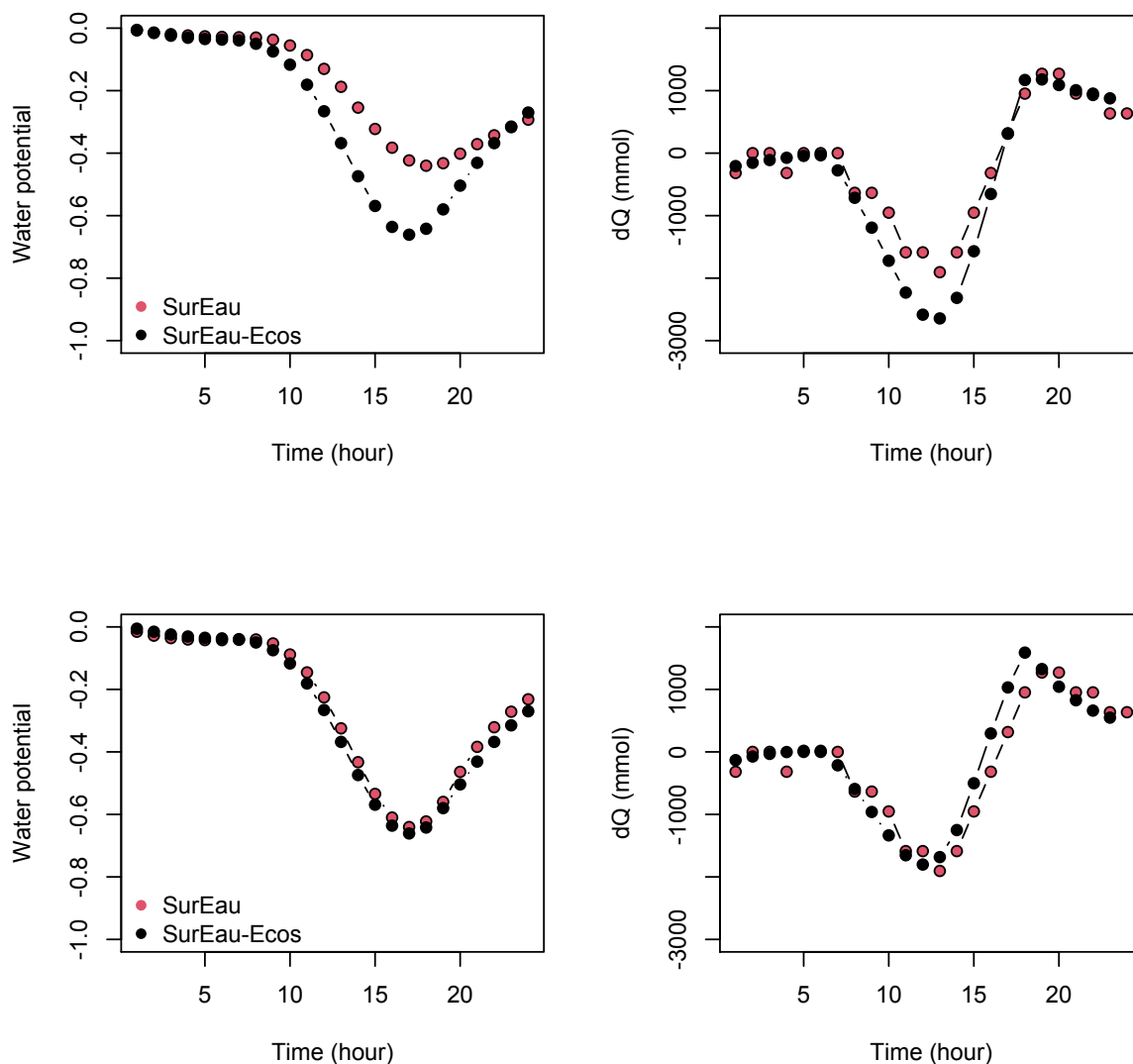
Fig. B6: Comparison of the water potential and the water discharge dynamics for the first day of simulation between the Trunk compartment of *SurEau* and the Stem compartment of *SurEau-Ecos* for two different parameterizations. In the upper panels *SurEau-Ecos* was parameterized with the stem symplasmic water volume computed as the sum of the symplasmic water volumes of the roots, trunk and branches of *SurEau*. In lower panels, the stem symplasmic water volume of SurEau-Ecos was considered to be equivalent to the trunk water volume of *SurEau* (see details in Tab. B2).

Appendix C: numerical schemes

C1. Explicit scheme

Let $\delta_L^{cav} = \begin{cases} 0, & if \ \psi_{LApo}^n \geq \psi_{LApo}^{mem} \ (no \ cavitation \ event) \\ 1, & if \ \psi_{LApo}^n < \psi_{LApo}^{mem} \ (cavitation \ event) \end{cases}$

And

Let $\delta_S^{cav} = \begin{cases} 0, & if \ \psi_{SApo}^n \geq \psi_{SApo}^{mem} \ (no \ cavitation \ event) \\ 1, & if \ \psi_{SApo}^n < \psi_{SApo}^{mem} \ (cavitation \ event) \end{cases}$

Applying the explicit scheme (Eq. 48 in main text) to the four water balance equations (Eq. 6 to 9 in main text):

Eq. 6 can be rearranged to determine ψ_{LApo}^{n+1}:

$$\psi_{LApo}^{n+1} = \psi_{LApo}^n + \frac{dt}{C_{LApo}}\Big(K_{SLApo}\big(\psi_{SApo}^n - \psi_{LApo}^n\big) + k_{LSym}\big(\psi_{LSym}^n - \psi_{LApo}^n\big) + \delta_L^{cav} K_L^{cav}\big(\psi_{LApo}^{cav} - \psi_{LApo}^n\big)\Big) \qquad \text{C1.1}$$

Similarly, Eq. 7 gives ψ_{SApo}^{n+1}:

$$\psi_{SApo}^{n+1} = \psi_{SApo}^n + \frac{dt}{C_{SApo}}\Bigg(K_{SLApo}\big(\psi_{LApo}^n - \psi_{SApo}^n\big) + K_{SSym}\big(\psi_{SSym}^n - \psi_{SApo}^n\big) + \delta_S^{cav} K_S^{cav}\big(\psi_{SApo}^{cav} - \psi_{SApo}^n\big)$$

$$+ \sum_j K_{soil_j S}\Big(\psi_{soil_j}^n - \psi_{SApo}^n\Big)\Bigg) \qquad \text{C1.2}$$

Then Eq. 8 and 9 give ψ_{LSym}^{n+1} and ψ_{TSym}^{n+1}

$$\psi_{LSym}^{n+1} = \psi_{LSym}^n + \frac{dt}{C_{LSym}}\Big(K_{LSym}\big(\psi_{LApo}^n - \psi_{LSym}^n\big) - Estom^{n+\frac{1}{2}} - Ecuti_L^{n+\frac{1}{2}}\Big) \qquad \text{C1.3}$$

$$\psi_{SSym}^{n+1} = \psi_{SSym}^n + \frac{dt}{C_{SSym}}\Big(K_{SSym}\big(\psi_{SApo}^n - \psi_{SSym}^n\big) - Ecuti_S^{n+\frac{1}{2}}\Big) \qquad \text{C1.4}$$

C2. Implicit scheme

By combining equations 6, 7, 8 and 9 with the implicit discretization (50), it is possible to analytically compute the unknown water potentials of each compartment at time $n+1$.

685 First, we eliminate ψ_{LSym}^{n+1} in equations 6 and 8 by summing $(6) + (8) \times \dfrac{K_{LSym}}{K_{LSym} + \frac{C_{LSym}}{dt} + \frac{E'^{n+\frac{1}{2}}}{2}}$ and re-organizing:

$$\frac{C_{LApo}}{dt}\left(\psi_{LApo}^{n+1} - \psi_{LApo}^n\right) + K_{SLApo}\left(\psi_{LApo}^{n+1} - \psi_{SApo}^{n+1}\right) + \frac{K_{LSym}\left(\frac{C_{LSym}}{dt} + \frac{E'^{n+\frac{1}{2}}}{2}\right)}{K_{LSym} + \frac{C_{LSym}}{dt} + \frac{E'^{n+\frac{1}{2}}}{2}}\left(\psi_{LApo}^{n+1} - \psi_{LSym}^n\right)$$
$$+ \delta_L^{cav} K_L^{cav}\left(\psi_{LApo}^{n+1} - \psi_{LApo}^{cav}\right) + \frac{K_{LSym}}{K_{LSym} + \frac{C_{LSym}}{dt} + \frac{E'^{n+\frac{1}{2}}}{2}}\left(E^{n+\frac{1}{2}} + Emin_L^{n+\frac{1}{2}}\right) = 0$$

C2.1

With $\delta_L^{cav} = \begin{cases} 0, & if \ \psi_{LApo}^{n+1} \geq \psi_{LApo}^{mem} \ (no\ new\ cavitation\ event) \\ 1, & if \ \psi_{LApo}^{n+1} < \psi_{LApo}^{mem} \ (new\ cavitation\ event) \end{cases}$

Let define intermediate variables to ease the resolution:

$$\widetilde{K_L} = \frac{C_{LApo}}{dt} + \frac{K_{LSym}\left(\frac{C_{LSym}}{dt} + \frac{E'^{n+\frac{1}{2}}}{2}\right)}{K_{LSym} + \frac{C_{LSym}}{dt} + \frac{E'^{n+\frac{1}{2}}}{2}} + \delta_L^{cav} K_L^{cav}$$

C2.2

and

$$\widetilde{\psi_L} = \frac{\frac{C_{LApo}}{dt}\psi_{LApo}^n + \frac{K_{LSym}\left(\frac{C_{LSym}}{dt} + \frac{E'^{n+\frac{1}{2}}}{2}\right)}{K_{LSym} + \frac{C_{LSym}}{dt} + \frac{E'^{n+\frac{1}{2}}}{2}}\psi_{LSym}^n + \delta_L^{cav} K_L^{cav} \psi_{LApo}^{cav}}{\widetilde{K_L}}$$

C2.3

and

$$\widetilde{E_L} = \frac{K_{LSym}}{K_{LSym} + \frac{C_{LSym}}{dt} + \frac{E'^{n+\frac{1}{2}}}{2}}\left(Estom^{n+\frac{1}{2}} + Ecuti_L^{n+\frac{1}{2}}\right)$$

C2.4

690

Now, equation C2.1 can be rewritten:

$$\widetilde{K_L}\left(\psi_{LApo}^{n+1} - \widetilde{\psi_L}\right) + K_{SLApo}\left(\psi_{LApo}^{n+1} - \psi_{SApo}^{n+1}\right) + \widetilde{E_L} = 0$$

C2.5

Similarly, eliminating ψ_{SSym}^{n+1} in equations 7 and 9 by summing $(7) + (9) \frac{1}{1+\frac{C_{SSym}}{k_{SSym} dt}}$ and re-organizing, this leads to:

$$\frac{C_{SApo}}{dt}\left(\psi_{SApo}^{n+1} - \psi_{SApo}^n\right) + K_{SLApo}\left(\psi_{SApo}^{n+1} - \psi_{LApo}^{n+1}\right) + \sum_j K_{soil_jS}\left(\psi_{SApo}^{n+1} - \psi_{soil_j}^n\right) + \frac{1}{\frac{1}{K_{SSym}} + \frac{dt}{C_{SSym}}}\left(\psi_{SApo}^{n+1} - \psi_{SSym}^n\right)$$
$$+ \delta_S^{cav} K_S^{cav}\left(\psi_{SApo}^{n+1} - \psi_{SApo}^{cav}\right) + \frac{Ecuti_S^{n+\frac{1}{2}}}{1 + \frac{C_{SSym}}{K_{SSym} dt}} = 0 \qquad \text{C2.6}$$

695 With $\delta_S^{cav} = \begin{cases} 0, & if\ \psi_{SApo}^{n+1} \geq \psi_{SApo}^{cav}\ (no\ new\ cavitation\ event) \\ 1, & if\ \psi_{SApo}^{n+1} < \psi_{SApo}^{cav}\ (new\ cavitation\ event) \end{cases}$

Similarly, defining:

$$\widetilde{K_S} = \frac{C_{SApo}}{dt} + \frac{1}{\frac{1}{K_{SSym}} + \frac{dt}{C_{SSym}}} + \sum_j K_{soil_jS} + \delta_S^{cav} K_S^{cav} \qquad \text{C2.7}$$

and

$$\widetilde{\psi_S} = \frac{\frac{C_{SApo}}{dt}\psi_{SApo}^n + \frac{1}{\frac{1}{K_{SSym}} + \frac{dt}{C_{SSym}}}\psi_{SSym}^n + \sum_j K_{soil_jS}\psi_{soil_j} + \delta_S^{cav} K_S^{cav}\psi_{SApo}^{cav}}{\widetilde{K_S}} \qquad \text{C2.8}$$

700 Equation C2.6 can be rewritten:

$$\widetilde{K_S}\left(\psi_{SApo}^{n+1} - \widetilde{\psi_S}\right) + K_{SLApo}\left(\psi_{SApo}^{n+1} - \psi_{LApo}^{n+1}\right) + \frac{Ecuti_S^{n+\frac{1}{2}}}{1 + \frac{C_{SSym}}{K_{SSym} dt}} = 0 \qquad \text{C2.9}$$

Now, we eliminate ψ_{SApo}^{n+1} from simplified equations C2.5 and C.9 by summing $(C5) + (C9) \times \frac{K_{SLApo}}{K_{SLApo}+\widetilde{K}}$ and re-organizing:

$$\widetilde{K_L}\left(\psi_{LApo}^{n+1} - \widetilde{\psi_L}\right) + \frac{K_{SLApo}\widetilde{K_S}}{K_{SLApo} + \widetilde{K_S}}\left(\psi_{LApo}^{n+1} - \widetilde{\psi_S}\right) + \widetilde{E_L} + \frac{K_{SLApo}}{K_{SLApo} + \widetilde{K_S}}\frac{Ecuti_S^{n+\frac{1}{2}}}{1 + \frac{C_{SSym}}{K_{SSym} dt}} = 0$$

Let

$$\widetilde{E_S} = \frac{K_{SLApo}}{K_{SLApo} + \widetilde{K_S}}\frac{Ecuti_S^{n+\frac{1}{2}}}{1 + \frac{C_{SSym}}{K_{SSym} dt}} \qquad \text{C2.10}$$

705

These equations can be combined to determine ψ_{LApo}^{n+1}, ψ_{SApo}^{n+1}, ψ_{LSym}^{n+1} and ψ_{SSym}^{n+1}

We can be rearranged to determine ψ_{LApo}^{n+1}:

$$\psi_{LApo}^{n+1} = \frac{\frac{K_{SLApo}\widetilde{K_S}}{K_{SLApo}+\widetilde{K_S}}\widetilde{\psi_S} + \widetilde{K_L}\widetilde{\psi_L} - [\widetilde{E_L} + \widetilde{E_S}]}{\frac{K_{SLApo}\widetilde{K_S}}{K_{SLApo}+\widetilde{K_S}} + \widetilde{K_L}}$$

C2.11

Knowing ψ_{LApo}^{n+1}, we can determine ψ_{SApo}^{n+1} from Equation C2.5:

$$\psi_{SApo}^{n+1} = \frac{(\widetilde{K_L} + K_{SLApo})\psi_{LApo}^{n+1} - \widetilde{K_L}\widetilde{\psi_L} + \widetilde{E_L}}{K_{SLApo}}$$

C2.12

In practice, because we don't know whether new cavitation events will occur during the time step, equations C2.2 and C2.3

710 and C2.7 and C2.8 are first computed assuming that δ_L^{cav} and δ_S^{cav} did not change since the last time step. This will be correct for most time steps, except those when cavitation either starts or ends. At this stage, we should hence check whether solutions ψ_{LApo}^{n+1} and ψ_{SApo}^{n+1} are below or above ψ_{LApo}^{cav} and ψ_{SApo}^{cav}, in order to eventually update δ_L^{cav} or δ_S^{cav} if needed. In case of change (for time steps exactly corresponding to begin or end of cavitation events), the computation should be done again with actualized values of δ_L^{cav} and δ_S^{cav}.

715 Finally, knowing ψ_{LApo}^{n+1}, we can solve ψ_{LSym}^{n+1} from Equation 8:

$$\psi_{LSym}^{n+1} = \frac{K_{LSym}\psi_{LApo}^{n+1} + \left(\frac{C_{LSym}}{dt} + \frac{E'^{n+\frac{1}{2}}}{2}\right)\psi_{LSym}^n - Estom^{n+\frac{1}{2}} - Ecuti_L^{n+\frac{1}{2}}}{K_{LSym} + \frac{C_{LSym}}{dt} + \frac{E'^{n+\frac{1}{2}}}{2}}$$

C2.13

And knowing ψ_{SApo}^{n+1}, we can solve ψ_{LSym}^{n+1} from Equation 9:

$$\psi_{SSym}^{n+1} = \frac{K_{SSym}\psi_{SApo}^{n+1} + \frac{C_{SSym}}{dt}\psi_{SSym}^n - Ecuti_S^{n+\frac{1}{2}}}{K_{SSym} + \frac{C_{SSym}}{dt}}$$

C2.14

C3. Semi-Implicit scheme

Let $\delta_L^{cav} = \begin{cases} 0, & if\ \psi_{LApo}^{n+1} \geq \psi_{LApo}^{mem}\ (no\ cavitation\ event) \\ 1, & if\ \psi_{LApo}^{n+1} < \psi_{LApo}^{mem}\ (cavitation\ event) \end{cases}$

720 And

With $\delta_S^{cav} = \begin{cases} 0, & if\ \psi_{SApo}^{n+1} \geq \psi_{SApo}^{cav}\ (no\ new\ cavitation\ event) \\ 1, & if\ \psi_{SApo}^{n+1} < \psi_{SApo}^{cav}\ (new\ cavitation\ event) \end{cases}$

By combining equations 6-9 with the semi-implicit solving (57), it leads to

725 For ψ_{LApo}^{n+1},

$$\psi_{LApo}^{n+1} = \alpha_{LApo}\psi_{LApo}^n + \left(1 - \alpha_{LApo}\right)\tilde{\psi}_{LApo}$$

$$\alpha_{LApo} = e^{-\frac{K_{TLApo}+K_{LSym}+\delta_L^{cav}k_L^{cav}}{C_{LApo}}dt} \quad and \quad \tilde{\psi}_{LApo} = \frac{K_{SLApo}\psi_{SApo}^n + K_{LSym}\psi_{LSym}^n + \delta_L^{cav}k_L^{cav}\psi_{LApo}^{cav}}{K_{SLApo} + k_{LSym} + \delta_L^{cav}k_L^{cav}}$$

C3.1

For ψ_{SApo}^{n+1},

$$\psi_{SApo}^{n+1} = \alpha_{SApo}\psi_{SApo}^n + \left(1 - \alpha_{SApo}\right)\tilde{\psi}_{SApo}$$

$$with \; \alpha_{SApo} = e^{-\frac{K_{SL}+K_{SSym}+\sum_j K_{soil_jS}+\delta_S^{cav}K_S^{cav}}{C_{SApo}}dt}$$

$$and \; \tilde{\psi}_{SApo} = \frac{K_{SLApo}\psi_{LApo}^n + K_{SSym}\psi_{SSym}^n + \sum_j K_{soil_jS}\psi_{soil_j}^n + \delta_S^{cav}K_S^{cav}\psi_{SApo}^{cav}}{K_{SLApo} + K_{SSym} + \sum_j K_{soil_jS} + \delta_S^{cav}K_S^{cav}}$$

C3.2

For ψ_{LSym}^{n+1},

$$\psi_{LSym}^{n+1} = \alpha_{LSym}\psi_{LSym}^n + \left(1 - \alpha_{LSym}\right)\tilde{\psi}_{LSym}$$

$$\alpha_{LSym} = e^{-\frac{k_{LSym}}{C_{LSym}}dt} \quad and \quad \tilde{\psi}_{LSym} = \frac{K_{LSym}\psi_{LApo}^n - Estom^n - Ecuti_L^n}{K_{LSym}}$$

C3.3

For ψ_{SSym}^{n+1},

$$\psi_{SSym}^{n+1} = \alpha_{SSym}\psi_{SSym}^n + \left(1 - \alpha_{SSym}\right)\tilde{\psi}_{SSym}$$

$$\alpha_{SSym} = e^{-\frac{K_{SSym}}{C_{SSym}}dt} \quad and \quad \tilde{\psi}_{SSym} = \frac{K_{SSym}\psi_{SApo}^n - Ecuti_S^n}{K_{SSym}}$$

C3.4

Code availability

The model code along with instructions on how to run the model version presented in this paper are available from https://doi.org/10.5281/zenodo.5878978

Author Contribution

JR led the writing of the manuscript with input from all authors. JR and NM coordinated the project. HC and JLD supervised the project. JR, NM, and FP developed the code and conducted the experiments. NM developed a preliminary version of the code. FP designed the numerical resolutions of the model with inputs from NM. All authors read and approved the manuscript.

Competing interests

The authors declare that they have no conflict of interest

Acknowledgments

References

Abram, N. J., Henley, B. J., Sen Gupta, A., Lippmann, T. J. R., Clarke, H., Dowdy, A. J., Sharples, J. J., Nolan, R. H., Zhang, T., Wooster, M. J., Wurtzel, J. B., Meissner, K. J., Pitman, A. J., Ukkola, A. M., Murphy, B. P., Tapper, N. J. and Boer, M. M.: Connections of climate change and variability to large and extreme forest fires in southeast Australia, Commun. Earth
750 Environ., 2(1), doi:10.1038/s43247-020-00065-8, 2021.

Adams, H. D., Zeppel, M. J. B., Anderegg, W. R. L., Hartmann, H., Landhäusser, S. M., Tissue, D. T., Huxman, T. E., Hudson, P. J., Franz, T. E., Allen, C. D., Anderegg, L. D. L., Barron-Gafford, G. A., Beerling, D. J., Breshears, D. D., Brodribb, T. J., Bugmann, H., Cobb, R. C., Collins, A. D., Dickman, L. T., Duan, H., Ewers, B. E., Galiano, L., Galvez, D. A., Garcia-Forner, N., Gaylord, M. L., Germino, M. J., Gessler, A., Hacke, U. G., Hakamada, R., Hector, A., Jenkins, M. W., Kane, J. M., Kolb,
755 T. E., Law, D. J., Lewis, J. D., Limousin, J.-M., Love, D. M., Macalady, A. K., Martínez-Vilalta, J., Mencuccini, M., Mitchell, P. J., Muss, J. D., O'Brien, M. J., O'Grady, A. P., Pangle, R. E., Pinkard, E. A., Piper, F. I., Plaut, J. A., Pockman, W. T., Quirk, J., Reinhardt, K., Ripullone, F., Ryan, M. G., Sala, A., Sevanto, S., Sperry, J. S., Vargas, R., Vennetier, M., Way, D. A., Xu, C., Yepez, E. A. and McDowell, N. G.: A multi-species synthesis of physiological mechanisms in drought-induced tree mortality, Nat. Ecol. Evol., 1(9), 1285–1291, doi:10.1038/s41559-017-0248-x, 2017.

760 Allen, C. D., Breshears, D. D. and McDowell, N. G.: On underestimation of global vulnerability to tree mortality and forest die-off from hotter drought in the Anthropocene, Ecosphere, 6(8), art129, doi:10.1890/ES15-00203.1, 2015.

Bartlett, M. K., Scoffoni, C. and Sack, L.: The determinants of leaf turgor loss point and prediction of drought tolerance of species and biomes: A global meta-analysis, Ecol. Lett., 15(5), 393–405, doi:10.1111/j.1461-0248.2012.01751.x, 2012.

Brodribb, T. J., Powers, J., Cochard, H. and Choat, B.: Hanging by a thread? Forests and drought, Science (80-.)., 368(6488),
765 261–266, doi:10.1126/science.aat7631, 2020.

De Cáceres, M., Martínez-Vilalta, J., Coll, L., Llorens, P., Casals, P., Poyatos, R., Pausas, J. G. and Brotons, L.: Coupling a water balance model with forest inventory data to predict drought stress: The role of forest structural changes vs. climate changes, Agric. For. Meteorol., 213, 77–90, doi:10.1016/j.agrformet.2015.06.012, 2015.

De Cáceres, M., Mencuccini, M., Martin-StPaul, N., Limousin, J. M., Coll, L., Poyatos, R., Cabon, A., Granda, V., Forner, A.,
770 Valladares, F. and Martínez-Vilalta, J.: Unravelling the effect of species mixing on water use and drought stress in Mediterranean forests: A modelling approach, Agric. For. Meteorol., 296(November 2020), doi:10.1016/j.agrformet.2020.108233, 2021.

Cheaib, A., Badeau, V., Boe, J., Chuine, I., Delire, C., Dufrêne, E., François, C., Gritti, E. S., Legay, M., Pagé, C., Thuiller, W., Viovy, N. and Leadley, P.: Climate change impacts on tree ranges: Model intercomparison facilitates understanding and
775 quantification of uncertainty, Ecol. Lett., 15(6), 533–544, doi:10.1111/j.1461-0248.2012.01764.x, 2012.

Choat, B., Brodribb, T. J., Brodersen, C. R., Duursma, R. A., López, R. and Medlyn, B. E.: Triggers of tree mortality under drought, Nature, 558(7711), 531–539, doi:10.1038/s41586-018-0240-x, 2018.

Christoffersen, B. O., Gloor, M., Fauset, S., Fyllas, N. M., Galbraith, D. R., Baker, T. R., Kruijt, B., Rowland, L., Fisher, R. A., Binks, O. J., Sevanto, S., Xu, C., Jansen, S., Choat, B., Mencuccini, M., McDowell, N. G. and Meir, P.: Linking hydraulic
780 traits to tropical forest function in a size-structured and trait-driven model (TFS v.1-Hydro), Geosci. Model Dev., 9(11), 4227–4255, doi:10.5194/gmd-9-4227-2016, 2016.

Cochard, H.: A new mechanism for tree mortality due to drought and heatwaves, bioRxiv, (February), 531632, doi:10.1101/531632, 2019.

Cochard, H., Pimont, F., Ruffault, J. and Martin-StPaul, N.: SurEau: a mechanistic model of plant water relations under
785 extreme drought, Ann. For. Sci., 78(2), doi:10.1007/s13595-021-01067-y, 2021.

Couvreur, V., Ledder, G., Manzoni, S., Way, D. A., Muller, E. B. and Russo, S. E.: Water transport through tall trees: A vertically explicit, analytical model of xylem hydraulic conductance in stems, Plant Cell Environ., 41(8), 1821–1839, doi:10.1111/pce.13322, 2018.

Cruiziat, P., Cochard, H. and Améglio, T.: Hydraulic architecture of trees: main concepts and results, Ann. For. Sci., 59(7),
790 723–752, doi:10.1051/forest:2002060, 2002.

Domec, J. C., Smith, D. D. and McCulloh, K. A.: A synthesis of the effects of atmospheric carbon dioxide enrichment on plant hydraulics: implications for whole-plant water use efficiency and resistance to drought, Plant Cell Environ., 40(6), 921–937, doi:10.1111/pce.12843, 2017.

Dufour-Kowalski, S., Courbaud, B., Dreyfus, P., Meredieu, C. and De Coligny, F.: Capsis: An open software framework and
795 community for forest growth modelling, in Annals of Forest Science., 2012.

Dutykh, D.: How to overcome the Courant-Friedrichs-Lewy condition of explicit discretizations?, Numer. Methods Diffus. Phenom. Build. Phys., 103–120, doi:10.1007/978-3-030-31574-0_5, 2016.

Fargeon, H., Pimont, F., Martin-StPaul, N., De Caceres, M., Ruffault, J., Barbero, R. and Dupuy, J. L.: Projections of fire danger under climate change over France: where do the greatest uncertainties lie?, Clim. Change, 160(3), 479–493,
800 doi:10.1007/s10584-019-02629-w, 2020.

Fatichi, S., Pappas, C. and Ivanov, V. Y.: Modeling plant–water interactions: an ecohydrological overview from the cell to the global scale, Wiley Interdiscip. Rev. Water, 3(3), 327–368, doi:10.1002/wat2.1125, 2016.

Feng, X., Ackerly, D. D., Dawson, T. E., Manzoni, S., Skelton, R. P., Vico, G. and Thompson, S. E.: The ecohydrological context of drought and classification of plant responses, Ecol. Lett., 21(11), 1723–1736, doi:10.1111/ele.13139, 2018.

805 Fettig, C. J., Mortenson, L. A., Bulaon, B. M. and Foulk, P. B.: Tree mortality following drought in the central and southern Sierra Nevada, California, U.S., For. Ecol. Manage., 432, 164–178, doi:10.1016/j.foreco.2018.09.006, 2019.

van Genuchten, M. T.: A closed-form equation for predicting the hydraulic conductivity of unsaturated soils, Soil Sci. Soc. Am. J., 44(5), 892, doi:10.2136/sssaj1980.03615995004400050002x, 1980.

Granier, A., Bréda, N., Biron, P. and Villette, S.: A lumped water balance model to evaluate duration and intensity of drought
810 constraints in forest stands, Ecol. Modell., 116(2–3), 269–283, doi:10.1016/S0304-3800(98)00205-1, 1999.

Hölttä, T., Cochard, H., Nikinmaa, E. and Mencuccini, M.: Capacitive effect of cavitation in xylem conduits: results from a dynamic model, Plant, cell \& Environ., 32(1), 10–21, 2009.

Jactel, H., Petit, J., Desprez-Loustau, M. L., Delzon, S., Piou, D., Battisti, A. and Koricheva, J.: Drought effects on damage by forest insects and pathogens: A meta-analysis, Glob. Chang. Biol., 18(1), 267–276, doi:10.1111/j.1365-2486.2011.02512.x,
815 2012.

Jarvis, P. G.: The interpretation of the variations in leaf water potential and stomatal conductance found in canopies in the field, Philos. Trans. R. Soc. London. B, Biol. Sci., 273(927), 593–610, doi:10.1098/rstb.1976.0035, 1976.

Jones, H. G.: Plants and microclimate: A quantitative approach to environmental plant physiology., Cambridge University Press., 2013.

820   De Kauwe, M. G., Medlyn, B. E., Ukkola, A. M., Mu, M., Sabot, M. E. B., Pitman, A. J., Meir, P., Cernusak, L. A., Rifai, S. W., Choat, B., Tissue, D. T., Blackman, C. J., Li, X., Roderick, M. and Briggs, P. R.: Identifying areas at risk of drought-induced tree mortality across South-Eastern Australia, Glob. Chang. Biol., 26(10), 0–2, doi:10.1111/gcb.15215, 2020.

Kennedy, D., Swenson, S., Oleson, K. W., Lawrence, D. M., Fisher, R., Lola da Costa, A. C. and Gentine, P.: Implementing Plant Hydraulics in the Community Land Model, Version 5, J. Adv. Model. Earth Syst., 11(2), 485–513,
825   doi:10.1029/2018MS001500, 2019.

Kotlarski, S., Keuler, K., Christensen, O. B., Colette, A., Déqué, M., Gobiet, A., Goergen, K., Jacob, D., Lüthi, D., Van Meijgaard, E. and others: Regional climate modeling on European scales: a joint standard evaluation of the EURO-CORDEX RCM ensemble, Geosci. Model Dev., 7, 1297–1333, 2014.

Lemaire, C., Blackman, C. J., Cochard, H., Menezes-Silva, P. E., Torres-Ruiz, J. M. and Herbette, S.: Acclimation of hydraulic
830   and morphological traits to water deficit delays hydraulic failure during simulated drought in poplar, Tree Physiol., 41(11), 2008–2021, 2021.

Li, L., Yang, Z., Matheny, A. M., Zheng, H., Swenson, S. C., Lawrence, D. M., Barlage, M., Yan, B., McDowell, N. G. and Leung, L. R.: Representation of Plant Hydraulics in the Noah-MP Land Surface Model: Model Development and Multi-scale Evaluation, J. Adv. Model. Earth Syst., doi:10.1029/2020ms002214, 2021.

835   López, R., Cano, F. J., Martin-StPaul, N. K., Cochard, H. and Choat, B.: Coordination of stem and leaf traits define different strategies to regulate water loss and tolerance ranges to aridity, New Phytol., 230(2), 497–509, 2021.

Mackay, D. S., Ahl, D. E., Ewers, B. E., Samanta, S., Gower, S. T. and Burrows, S. N.: Physiological tradeoffs in the parameterization of a model of canopy transpiration, Adv. Water Resour., 26(2), 179–194, doi:10.1016/S0309-1708(02)00090-8, 2003.

840   Mantova, M., Menezes-Silva, P. E., Badel, E., Cochard, H. and Torres-Ruiz, J. M.: The interplay of hydraulic failure and cell vitality explains tree capacity to recover from drought, Physiol. Plant., ppl.13331, doi:10.1111/ppl.13331, 2021.

Martin-StPaul, N., Delzon, S. and Cochard, H.: Plant resistance to drought depends on timely stomatal closure, edited by H. Maherali, Ecol. Lett., 20(11), doi:10.1111/ele.12851, 2017.

Mcdowell, N., Sapes, G., Pivovaroff, A., Adams, H., Allen, C., Anderegg, W., Arend, M., Breshears, D., Brodribb, T., Choat,
845   B., Cochard, H., De Caceres, M., DE Kauwe, M., Grossiord, C., Hammond, W., Hartmann, H., Hoch, G., Kahmen, A., Klein, T., Mackay, D., Montova, M., Martínez-Vilalta, J., Medlyn, B., Mencuccini, M., Nardini, A., Oliveira, R., Sala, A., Tissue, D., Torres-Ruiz, J., Trowbridge, A., Trugman, A., Wiley, E. and Xu, C.: Mechanisms of woody plant mortality under rising drought, CO2, and vapor pressure deficit., Nat. Rev. Earth Environ., (in press), n.d.

McDowell, N. G., Brodribb, T. J. and Nardini, A.: Hydraulics in the 21st century, New Phytol., 224(2), 537–542,
850   doi:10.1111/nph.16151, 2019.

Meir, P., Meir, P., Mencuccini, M. and Dewar, R. C.: Tansley insight Drought-related tree mortality : addressing the gaps in understanding and prediction, New Phytol., 2015.

Mencuccini, M., Manzoni, S. and Christoffersen, B.: Modelling water fluxes in plants: from tissues to biosphere, New Phytol., 222(3), 1207–1222, doi:10.1111/nph.15681, 2019.

855   Mouillot, F., Rambal, S. and Lavorel, S.: A generic process-based SImulator for meditERRanean landscApes (SIERRA): design and validation exercises, For. Ecol. Manage., 147(1), 75–97 [online] Available from: http://www.sciencedirect.com/science/article/B6T6X-430G282-9/2/ba1abdd5b7947b8d5191d4590d145715, 2001.

Nolan, R. H., Blackman, C. J., de Dios, V. R., Choat, B., Medlyn, B. E., Li, X., Bradstock, R. A. and Boer, M. M.: Linking Forest Flammability and Plant Vulnerability to Drought, Forests, 11(7), 779, doi:10.3390/f11070779, 2020.

860   Pammenter, N. W. and Vander Willigen, C.: A mathematical and statistical analysis of the curves illustrating vulnerability of xylem to cavitation, Tree Physiol., 18(8_9), 589–593, 1998.

R Core Team: R: A Language and Environment for Statistical Computing, [online] Available from: http://www.r-project.org/, 2020.

Rambal, S.: The differential role of mechanisms for drought resistance in a Mediterranean evergreen shrub: a simulation approach, Plant. Cell Environ., 16(1), 35–44, doi:10.1111/j.1365-3040.1993.tb00842.x, 1993.

Rowland, L., Martínez-Vilalta, J. and Mencuccini, M.: Hard times for high expectations from hydraulics: predicting drought-induced forest mortality at landscape scales remains a challenge, New Phytol., 230(5), 1685–1687, doi:10.1111/nph.17317, 2021.

Ruffault, J., Martin-StPaul, N. K. N., Rambal, S. and Mouillot, F.: Differential regional responses in drought length, intensity and timing to recent climate changes in a Mediterranean forested ecosystem, Clim. Change, 117(1–2), 103–117, doi:10.1007/s10584-012-0559-5, 2013.

Ruffault, J., Martin-StPaul, N. K., Duffet, C., Goge, F. and Mouillot, F.: Projecting future drought in Mediterranean forests: Bias correction of climate models matters!, Theor. Appl. Climatol., 117(1), 113–122, doi:10.1007/s00704-013-0992-z, 2014.

Ruffault, J., Curt, T., Martin-StPaul, N. K., Moron, V. and Trigo, R. M.: Extreme wildfire events are linked to global-change-type droughts in the northern Mediterranean, Nat. Hazards Earth Syst. Sci., 18(3), 847–856, doi:10.5194/nhess-18-847-2018, 2018.

Ruffault, J., Curt, T., Moron, V., Trigo, R. M., Mouillot, F., Koutsias, N., Pimont, F., Martin-StPaul, N. K., Barbero, R., Dupuy, J. L., Russo, A. and Belhadj-Kheder, C.: Increased likelihood of heat-induced large wildfires in the Mediterranean Basin, Sci. Rep., 10(1), 13790, doi:10.1101/2020.01.09.896878, 2020.

Schuldt, B., Buras, A., Arend, M., Vitasse, Y., Beierkuhnlein, C., Damm, A., Gharun, M., Grams, T. E. E., Hauck, M., Hajek, P., Hartmann, H., Hiltbrunner, E., Hoch, G., Holloway-Phillips, M., Körner, C., Larysch, E., Lübbe, T., Nelson, D. B., Rammig, A., Rigling, A., Rose, L., Ruehr, N. K., Schumann, K., Weiser, F., Werner, C., Wohlgemuth, T., Zang, C. S. and Kahmen, A.: A first assessment of the impact of the extreme 2018 summer drought on Central European forests, Basic Appl. Ecol., 45, 86–103, doi:10.1016/j.baae.2020.04.003, 2020.

Seidl, R., Schelhaas, M.-J., Rammer, W. and Verkerk, P. J.: Increasing forest disturbances in Europe and their impact on carbon storage, Nat. Clim. Chang., 4(9), 806–810, 2014.

Sobol, I. M.: Global sensitivity indices for nonlinear mathematical models and their Monte Carlo estimates, Math. Comput. Simul., 55(1–3), 271–280, 2001.

Sperry, J. S., Adler, F. R., Campbell, G. S. and Comstock, J. P.: Limitation of plant water use by rhizosphere and xylem conductance: results from a model, Plant, Cell Environ., 21(4), 347–359, doi:10.1046/j.1365-3040.1998.00287.x, 1998.

Sperry, J. S., Venturas, M. D., Anderegg, W. R. L., Mencuccini, M., Mackay, D. S., Wang, Y. and Love, D. M.: Predicting stomatal responses to the environment from the optimization of photosynthetic gain and hydraulic cost, Plant, cell \& Environ., 40(6), 816–830, 2017.

Sterck, F., Markesteijn, L., Schieving, F. and Poorter, L.: Functional traits determine trade-offs and niches in a tropical forest community, Proc. Natl. Acad. Sci. U. S. A., 108(51), 20627–20632, doi:10.1073/pnas.1106950108, 2011.

Trenberth, K. E., Dai, A., Van Der Schrier, G., Jones, P. D., Barichivich, J., Briffa, K. R. and Sheffield, J.: Global warming and changes in drought, Nat. Clim. Chang., 4(1), 17–22, 2014.

Trugman, A. T., Anderegg, L. D. L., Anderegg, W. R. L., Das, A. J. and Stephenson, N. L.: Why is Tree Drought Mortality so Hard to Predict?, Trends Ecol. Evol., 36(6), 520–532, doi:10.1016/j.tree.2021.02.001, 2021.

Tuzet, A., Granier, A., Betsch, P., Peiffer, M. and Perrier, A.: Modelling hydraulic functioning of an adult beech stand under non-limiting soil water and severe drought condition, Ecol. Modell., 348(March), 56–77, doi:10.1016/j.ecolmodel.2017.01.007, 2017.

Tyree, M. T. and Hammel, H. T.: The Measurement of the turgor pressure and the water relations of plants by the pressure-

bomb technique, J. Exp. Bot., 23(1), 267–282, doi:10.1093/jxb/23.1.267, 1972.

905 Venturas, M. D., Todd, H. N., Trugman, A. T. and Anderegg, W. R. L.: Understanding and predicting forest mortality in the western United States using long-term forest inventory data and modeled hydraulic damage, New Phytol., doi:10.1111/nph.17043, 2020.

Vidal, J. P., Martin, E., Franchistéguy, L., Baillon, M. and Soubeyroux, J. M.: A 50 year high resolution atmospheric reanalysis over France with the Safran system, Int. J. Climatol., 30(11), 1627–1644, 2010.

910 Wang, Y., Sperry, J. S., Anderegg, W. R. L. L., Venturas, M. D. and Trugman, A. T.: A theoretical and empirical assessment of stomatal optimization modeling, New Phytol., 227(2), 311–325, doi:10.1111/nph.16572, 2020.

Williams, M., Rastetter, E. B., Fernandes, D. N., Goulden, M. L., Wofsy, S. C., Shaver, G. R., Melillo, J. M., Munger, J. W., Fan, S. M. and Nadelhoffer, K. J.: Modelling the soil-plant-atmosphere continuum in a Quercus-acer stand at Harvard forest: The regulation of stomatal conductance by light, nitrogen and soil/plant hydraulic properties, Plant, Cell Environ., 19(8), 911–
915 927, doi:10.1111/j.1365-3040.1996.tb00456.x, 1996.

Xu, X., Medvigy, D., Powers, J. S., Becknell, J. M. and Guan, K.: Diversity in plant hydraulic traits explains seasonal and inter-annual variations of vegetation dynamics in seasonally dry tropical forests, New Phytol., 212(1), 80–95, doi:10.1111/nph.14009, 2016.